Escola de Camins
Escola Tècnica Superior d'Enginyeria de Camins, Canals i Ports
UPC BARCELONATECH

TREBALL FINAL DE MÀSTER

THE FACE-CENTERED FINITE VOLUME METHOD (FCFV) FOR STEADY-STATE INCOMPRESSIBLE NAVIER-STOKES EQUATIONS

Treball realitzat per:
Shushu Qin

Dirigit per:
Dr. Matteo Giacomini
Prof. Antonio Huerta
Dr. Rubén Sevilla

Grau en:
Erasmus Mundus M.Sc. in Computational Mechanics

Barcelona, **14 June 2019**

Departament: **Laboratori de Càlcul Numèric**

The Face-Centered Finite Volume Method (FCFV) for Steady-State Incompressible Navier-Stokes Equations

Author:
Shushu Qin

Supervisor:
Dr. Matteo Giacomini
Prof. Antonio Huerta
Dr. Rubén Sevilla

A thesis submitted for the degree of
Master of Science in Computational Mechanics

2019

Abstract

Computational Fluid Dynamics (CFD) techniques are a widespread tool to simulate complex flow problems, e.g. in the field of aerospace and automotive industries, biomedical, chemical, and marine engineering. During the last decades, a great effort has been devoted to validate numerical results provided by CFD simulations by means of experimental tests. Hence, CFD tools are currently integrated in daily production routines of industries owing to their reliability and their limited cost compared to experimental tests.

Finite volume (FV) methods are among the most popular CFD solvers in the industry. FV methods naturally enforce conservation of physical laws and provide robust and efficient solvers suitable for overnight computations of large problems. Classical FV methods, e.g. the cell-centered (CCFV) and vertex-centered (VCFV) approaches, are known to suffer from loss of accuracy in presence of stretched and irregular meshes. On the contrary, the recently proposed face-centered (FCFV) paradigm is robust to mesh stretching and deformation, is LBB-compliant and provides first-order accuracy for velocity, pressure and strain tensor with no need of flux reconstruction.

In this work, an FCFV method for the steady-state incompressible Navier-Stokes equations is proposed. Voigt notation is utilized to enforce the symmetry of the stress tensor so that physical tractions are applied on the Neumann boundary. A detailed mathematical derivation is provided and numerical examples are presented to illustrate the accuracy and efficiency of the proposed methodology on both synthetic and benchmark test cases from the literature.

Keywords: finite volume method, face-centered, hybridisable discontinuous Galerkin, lowest order approximation, incompressible Navier-Stokes equations

Acknowledgements

I still remember my first day of master studies in Swansea. It was a rainy windy day and I was dressed in a thick deep-green coat standing among the red buildings. The British may not call it rain but drizzle or sprinkle. Anyway, now the master ends in the sunshine of Barcelona. Look to the past, I need to thank many people for their assistance, encouragement, attention and kindness in my journey towards this degree.

This master thesis would not have been successfully accomplished without the amazing professors who have taught me during the past two years.I would like to thank **Dr. Rubén Sevilla**, who leads me to the field of Computational Mechanics. He gives me insightful guidance in deciding the topic of my master thesis and shows me the way ahead. I want to express my sincere gratitude to **Prof. Antonio J. Gil**, who taught us continuum mechanics in Swansea University. I was impressed by his enthusiasm in teaching and admire his passion in academic research. He excites students' interests and stimulates their creativity in class. Even if I was in UPC, he was also available to help with the problems in study.

I want to express my sincere gratitude to **Prof. Antonio Huerta** who offers me the opportunity to work on this interesting project and **Dr. Matteo Giacomini** who explains the theory, shares credible ideas, dispels my confusion, and encourages me to break through obstacles in accomplishing the thesis. I need to acknowledge my colleague **Jordi Vila Pérez**. He is always available for my questions.

I also want to thank my classmates and friends – **Raúl Bravo** and **Arthur Lustman**, who encouraged me when I was struggling with the project. Bravo and Arthur never let things get dull or boring and bring me bright mood every day. I feel lucky to meet them in my master.

My acknowledgement would be incomplete without thanking my dear parents – **Ling Ge** and **Jianhua Qin**. They always back me up and give me confidence to try any possibility. Their unwavering and unselfish love is my biggest source of strength and reminds me never give up no matter what kind of challenges or difficulties I go through.

Many thanks!

Contents

List of Figures

List of Tables

Chapter 1

Introduction

1.1 Background

With the rise of computers and computing power, Computational Fluid Dynamics (CFD) firstly appeared in the 1960s in the aerospace industry [2]. In the past decades, CFD has been an active field of study and many methodologies were devised. Concerning spatial discretisation, we can at first divide the schemes in three main categories: finite difference, finite volume, and finite element. The finite volume method (FVM) has great advantages as it directly utilises the conservation laws. Nowadays, it is the most widely spread methodology in the industry. There are several possibilities of defining the shape and position of the control volume with respect to the grid. The two most popular approaches are the so called cell-centered finite volume (CCFV) method [3] and the vertex-centered finite volume (VCFV) method [4] depending on the localisation of the unknowns in the computational mesh.

CCFV method defines unknowns at the centroid of the mesh cells [5]. It has the limitation of nontrivial approximation of the gradient of the solution. Several techniques are developed to resolve this problem such as node averaging or least squares scheme [6, 7]. In all these cases, the accuracy of the reconstruction is dependent on the mesh quality. Some approaches fail to achieve first-order convergence of solution gradient on highly stretched and deformed grids [8].

VCFV method defines unknowns at the cell nodes [9]. The reconstruction of solution gradient is also required so it has the same disadvantage of poor performance under highly stretched and deformed grids [6]. Moreover, both approaches use constant approximation for velocity and pressure, thus requiring the introduction of stabilisation terms to avoid spurious pressure modes [10].

Apart from FV methods, finite elements(FE) methods are also widely used in the simulation of fluids. FE methods have been developed in 1950s since M. J. (Jon) Turner at Boeing invented the so called Direct Stiffness Method [11]. It was firstly applied in structural

engineering and has emerged as one of the most powerful methods so far devised. The success of FE methods in structural mechanics and other problems governed by self-adjoint elliptic or parabolic partial differential equations has a strong impetus for the application of this method in the simulation of fluids. Compared with FV methods, FE methods have the advantages that the solution in each element can be easily constructed from the basis functions. However, solving viscous incompressible flows leads to three numerical difficulties [10] when using FE methodology.

The first difficulty is related to the incompressibility of the flow. In this case, pressure acts as a Lagrange multiplier of the incompressibility constraint. It will lead to a saddle-point problem which requires an $inf - sup$ condition to be satisfied in order to guarantee the well-posedness of the problem. It can be solved either by resorting to LBB-compliant FE pairs or by introducing stabilisation terms. A common strategy for LBB-compliant approximation relies on using different interpolation spaces for the variables, namely pressure being interpolated with a lower order polynomial than the velocity field [12–14]. Another remedy is the penalty method [15–17], which may be interpreted as enabling a relaxation of the incompressible constraint. The problem can also be resolved by the augmented method [18–20], which enriches the formulation with some residual terms arising from the constitutive, equilibrium equations and the Dirichlet boundary condition.

The second difficulty comes from the nonlinear convection term. Two common approaches are the Picard scheme and the Newton-Raphson scheme. The Newton-Raphson method is generally capable of reaching the convergence of the equations in a small number of iterations [21–23] while the Picard method converges linearly. In this project, the Newton's method is applied to solve the nonlinear system of Navier-Stokes equations.

The presence of convection operators also leads to the third difficulty in solving the Navier-Stokes equations. When the convection influence dominates over the diffusion, solutions to these problems by the Galerkin methods are often corrupted by spurious node-to-node oscillations. There are two main remedies for the deficiency of the FE method. One is by adding diffusion to the numerical scheme an the other is based on an upwind approximation of the convective term such as the Streamline-Upwind Petrov-Galerkin (SUPG) and the Galerkin/Least-squares (GLS) methods [10]. In 1973, an ingenious technique called discontinuous Galerkin (DG) was firstly introduced by Reed and Hill [24]. DG stabilizes convection-dominated problems by appropriately defining numerical fluxes and high-order accuracy can thus be obtained. The main drawback of DG is the duplication of degrees of freedom and the consequent increase of computational cost. A possible workaround is represented by the hybridizable discontinuous Galerkin (HDG) method [25–28].

HDG relies on the mixed hybrid formulation with discontinuous approximations element by element. The degrees of freedom in each mesh elements, namely velocity, pressure and strain tensor, are statically condensed and written in terms of the global unknown, the hybrid velocity on the mesh faces. FCFV [29, 30], is obtained as a lowest-order HDG method in which velocity, pressure and stress tensor are approximated as constant values element-by-element whereas the hybrid velocity is discretised using a constant value on

each face. Thus, FCFV inherits the optimal convergence properties of HDG, providing first-order accuracy for velocity, pressure and strain tensor without the need to perform flux reconstruction.

1.2 Aim of the project

The aim of this MSc Thesis is to implement an efficient FCFV solver for steady-state incompressible Navier-Stokes equations and apply it to the simulation of the viscous laminar flow problems of industrial interest. Voigt notation is exploited to strongly enforce the symmetry of the stress tensor and to enforce physical tractions on Neumann boundaries. The proposed methodology is implemented using MATLAB®. Both synthetic and benchmark test cases from the literature are studied to validate the proposed method and verify the optimal first-order convergence rates of velocity, pressure and strain tensor.

1.3 Outline

The manuscript consists of the following sections:

- *Chapter One: Introduction.* This chapter provides a general setting of the context, with a short overview of the background and the target of the thesis.
- *Chapter Two: FCFV method for the Stokes equations.* This chapter presents the derivation of the FCFV method for the Stokes equations. A brief introduction to Voigt notation for symmetric second-order tensors is included. The integral forms of FCFV local and global problems are detailed. Numerical studies are carried out to validate of the method and verify optimal convergence rates of the discrete variables.
- *Chapter Three: FCFV method for the Oseen equations.* This chapter presents the derivation of the FCFV method for the Oseen equations, which is a linearized form of Navier-Stokes equations. It serves as a stepping stone to solve the Navier-Stokes equation. The structure of the chapter is similar to what has been presented in Chapter Two.
- *Chapter Four: FCFV method for the Navier-Stokes equations.* This chapter presents the derivation of the FCFV method for the Navier-Stokes equations. The derivation of the integral forms and matrix forms is similar to what was done in the Oseen problem. Moreover, the Newton-Raphson method is introduced here in order to solve the nonlinear global system. After verifying the optimal convergence rate of the method using a synthetic example, a classic benchmark test for incompressible laminar Navier-Stokes solver, namely the lid-driven cavity, is studied for different values of the Reynolds number.

- *Chapter Five: Conclusion.* This chapter provides a summary of the project and the future developments of the current work.

Chapter 2

FCFV method for the Stokes equations

In this section, the stationary Stokes problem is considered. It is correspondent to steady highly diffusive Navier-Stokes equations, where the velocity is very small compared with viscous forces so that the convective term can be neglected. Voigt notation is introduced in the strong form to apply real tractions at the Neumann boundary. The local and global FCFV problems are written in integral form and the corresponding linear system is derived. Two 2D numerical tests are presented to validate the methodology.

2.1 Governing equations of the Stokes flow

Let $\Omega \in \mathbb{R}^{\mathtt{n_{sd}}}$ be an open bounded domain with boundary $\partial\Omega = \overline{\Gamma}_D \cup \overline{\Gamma}_N$, where $\overline{\Gamma}_N$ and $\overline{\Gamma}_D$ are Dirichlet and Neumann boundaries respectively, $\overline{\Gamma}_D \cap \overline{\Gamma}_N = \emptyset$, and $\mathtt{n_{sd}}$ is the number of spatial dimensions. Consider a Stokes problem with Dirichlet and Neumann boundary conditions in Ω. The Cauchy formulation of the Stokes problem reads as

$$\begin{cases} -\boldsymbol{\nabla}\cdot\boldsymbol{\sigma} = \boldsymbol{s} & \text{in } \Omega, \\ \boldsymbol{\nabla}\cdot\boldsymbol{u} = 0 & \text{in } \Omega, \\ \boldsymbol{u} = \boldsymbol{u}_D & \text{on } \Gamma_D, \\ \boldsymbol{\sigma}\cdot\boldsymbol{n} = \boldsymbol{t} & \text{on } \Gamma_N, \end{cases} \tag{2.1.1}$$

For a Newtonian fluid, the stress tensor and the strain rate tensor are assumed to be linearly related. The Cauchy stress tensor of a Stokes flow is define as [10]

$$\boldsymbol{\sigma} = 2\nu\boldsymbol{\nabla}^{\mathtt{s}}\boldsymbol{u} - p\boldsymbol{I}_{\mathtt{n_{sd}}} \tag{2.1.2}$$

where $(\boldsymbol{u}, p)$ represents the velocity and pressure fields associated with the problem, ν is the viscosity of the fluid, $\boldsymbol{\nabla}^{\mathtt{s}}\boldsymbol{u} = \frac{1}{2}\boldsymbol{\nabla}\boldsymbol{u} + \frac{1}{2}(\boldsymbol{\nabla}\boldsymbol{u})^T$, and $\boldsymbol{I}_{\mathtt{n_{sd}}}$ is the identity tensor.

Hence, the strong form of the boundary value Stokes equation can be rewritten as

$$\begin{cases} -\boldsymbol{\nabla}\cdot(2\nu\boldsymbol{\nabla}^{\mathrm{s}}\boldsymbol{u}-p\boldsymbol{I}_{\mathtt{n_{sd}}}) = \boldsymbol{s} & \text{in } \Omega, \\ \boldsymbol{\nabla}\cdot\boldsymbol{u} = 0 & \text{in } \Omega, \\ \boldsymbol{u} = \boldsymbol{u}_D & \text{on } \Gamma_D, \\ \boldsymbol{n}\cdot\big(2\nu\boldsymbol{\nabla}^{\mathrm{s}}\boldsymbol{u}-p\boldsymbol{I}_{\mathtt{n_{sd}}}\big) = \boldsymbol{t} & \text{on } \Gamma_N, \end{cases} \tag{2.1.3}$$

where $\boldsymbol{n}$ is the outward unit normal vector to $\partial\Omega$, and $\boldsymbol{s}$, $\boldsymbol{u}_D$ and $\boldsymbol{t}$ are, respectively, the volumetric source term, the Dirichlet boundary datum to impose the value of the velocity on Γ_D and the Neumann boundary condition for the traction force on Γ_N. The first equation in Equation (2.1.3) is the conservation law of momentum. The second equation represents conservation of mass and imposes incompressibility of the flow.

It's worth mentioning that many researchers use the Laplace form of the Stokes flow by rewriting the momentum equation as [10]

$$-\boldsymbol{\nabla}\cdot(\nu\boldsymbol{\nabla}\boldsymbol{u})+\boldsymbol{\nabla}p = \boldsymbol{s} \qquad \text{in } \Omega \tag{2.1.4}$$

by exploiting the incompressibility $\boldsymbol{\nabla}\cdot\boldsymbol{u} = 0$. In this case, in the Neumann boundary condition the real traction is replaced by the natural boundary condition for the Laplace form:

$$\boldsymbol{n}\cdot\big(\nu\boldsymbol{\nabla}\boldsymbol{u}-p\boldsymbol{I}_{\mathtt{n_{sd}}}\big) = \boldsymbol{t} \qquad \text{on } \Gamma_N, \tag{2.1.5}$$

which is called pseudo-traction. The Laplace form and strong form of the momentum equation are equivalent while those of the Neumann boundary condition are not. The inconsistency with physics may cause some problems in application. In the paper by Limache et al. [31], spurious results are observed in the simulation of a fluid-structure-interation problem due to the simplification of boundary condition. Therefore, physical tractions are applied on the Neumann boundary in this project.

Giacomini et al. [32] showed that with the help of Voigt notation, the imposition of physical tractions is straightforward in the context of viscous flows. In this thesis, we will exploit Voigt notation to define a symmetric mixed variable for FCFV representing the strain tensor following the framework in [30].

2.2 Voigt notation for symmetric second-order tensors

The idea of Voigt notation is to store a symmetric tensor in a vectorial format by appropriately rearranging its diagonal and off-diagonal components.

Owing to the symmetry of the strain rate tensor, $\boldsymbol{\nabla}^{\mathrm{s}}\boldsymbol{u}$ can be fully represented by $\mathtt{m_{sd}} = \mathtt{n_{sd}}(\mathtt{n_{sd}}+1)/2$ components (i.e. three in 2D and six in 3D). According to the arrangement

proposed by Fish and Belytschko [33], the following column vector is used for vectorising the strain rate tensor

$$\boldsymbol{e}_{\mathtt{v}} := \begin{cases} \begin{bmatrix} e_{11},\ e_{22},\ e_{12} \end{bmatrix}^T & \text{in 2D,} \\ \begin{bmatrix} e_{11},\ e_{22},\ e_{33},\ e_{12},\ e_{13},\ e_{23} \end{bmatrix}^T & \text{in 3D.} \end{cases} \tag{2.2.1}$$

The components of the strain rate in Equation (2.2.1) are

$$e_{ij} := \frac{\partial u_i}{\partial x_j} + (1 - \delta_{ij}) \frac{\partial u_j}{\partial x_i}, \quad \text{for } i, j = 1, \ldots, \mathtt{n_{sd}} \text{ and } i \leq j \ , \tag{2.2.2}$$

where δ_{ij} is the classical Kronecker delta. The strain rate tensor $\boldsymbol{\nabla}^{\mathtt{s}}\boldsymbol{u}$ is expressed with components in $\boldsymbol{e}_{\mathtt{v}}$ by multiplying the off-diagonal terms $e_{ij},\ i \neq j$ with a factor $1/2$

$$\boldsymbol{\nabla}^{\mathtt{s}}\boldsymbol{u} := \begin{cases} \begin{bmatrix} e_{11} & e_{12}/2 \\ e_{12}/2 & e_{22} \end{bmatrix} & \text{in 2D,} \\ \begin{bmatrix} e_{11} & e_{12}/2 & e_{13}/2 \\ e_{12}/2 & e_{22} & e_{23}/2 \\ e_{13}/2 & e_{23}/2 & e_{33} \end{bmatrix} & \text{in 3D.} \end{cases} \tag{2.2.3}$$

Thus, the strain rate tensor can be written as $\boldsymbol{e}_{\mathtt{v}} = \boldsymbol{\nabla}_{\mathtt{s}}\boldsymbol{u}$ by introducing the $\mathtt{m_{sd}} \times \mathtt{n_{sd}}$ matrix

$$\boldsymbol{\nabla}_{\mathtt{s}} := \begin{cases} \begin{bmatrix} \partial/\partial x_1 & 0 & \partial/\partial x_2 \\ 0 & \partial/\partial x_2 & \partial/\partial x_1 \end{bmatrix}^T & \text{in 2D,} \\ \begin{bmatrix} \partial/\partial x_1 & 0 & 0 & \partial/\partial x_2 & \partial/\partial x_3 & 0 \\ 0 & \partial/\partial x_2 & 0 & \partial/\partial x_1 & 0 & \partial/\partial x_3 \\ 0 & 0 & \partial/\partial x_3 & 0 & \partial/\partial x_1 & \partial/\partial x_2 \end{bmatrix}^T & \text{in 3D.} \end{cases} \tag{2.2.4}$$

The stress tensor can be rewritten as $\boldsymbol{\sigma}_{\mathtt{v}} = \mathbf{D}\boldsymbol{\nabla}_{\mathtt{s}}\boldsymbol{u} - \mathbf{E}p$, where the vector $\mathbf{E} \in \mathbb{R}^{\mathtt{m_{sd}}}$ and the matrix $\mathbf{D} \in \mathbb{R}^{\mathtt{m_{sd}} \times \mathtt{m_{sd}}}$ read as

$$\mathbf{E} := \begin{cases} \begin{bmatrix} 1,\ 1,\ 0 \end{bmatrix}^T & \text{in 2D,} \\ \begin{bmatrix} 1,\ 1,\ 1,\ 0,\ 0,\ 0 \end{bmatrix}^T & \text{in 3D.} \end{cases} \qquad \mathbf{D} := \begin{cases} \begin{bmatrix} 2\nu \boldsymbol{I}_{\mathtt{n_{sd}}} & \mathbf{0}_{\mathtt{n_{sd}} \times 1} \\ \mathbf{0}^T_{\mathtt{n_{sd}} \times 1} & \nu \end{bmatrix} & \text{in 2D,} \\ \begin{bmatrix} 2\nu \boldsymbol{I}_{\mathtt{n_{sd}}} & \mathbf{0}_{\mathtt{n_{sd}}} \\ \mathbf{0}_{\mathtt{n_{sd}}} & \nu \boldsymbol{I}_{\mathtt{n_{sd}}} \end{bmatrix} & \text{in 3D.} \end{cases} \tag{2.2.5}$$

The Neumann boundary condition applied on Γ_N can be written as $\mathbf{N}^T\boldsymbol{\sigma}_{\mathtt{v}} = \boldsymbol{t}$ by intro-

ducing the $\mathtt{m_{sd}} \times \mathtt{n_{sd}}$ matrix

$$\mathbf{N} := \begin{cases} \begin{bmatrix} n_1 & 0 & n_2 \\ 0 & n_2 & n_1 \end{bmatrix}^T & \text{in 2D,} \\ \begin{bmatrix} n_1 & 0 & 0 & n_2 & n_3 & 0 \\ 0 & n_2 & 0 & n_1 & 0 & n_3 \\ 0 & 0 & n_3 & 0 & n_1 & n_2 \end{bmatrix}^T & \text{in 3D,} \end{cases} \tag{2.2.6}$$

Rewrite the strong form of the Stokes equation using the Voigt notation, we have

$$\begin{cases} -\boldsymbol{\nabla}_{\mathtt{s}}^T(\mathbf{D}\boldsymbol{\nabla}_{\mathtt{s}}\boldsymbol{u} - \mathbf{E}p) = \boldsymbol{s} & \text{in } \Omega, \\ \mathbf{E}^T\boldsymbol{\nabla}_{\mathtt{s}}\boldsymbol{u} = 0 & \text{in } \Omega, \\ \boldsymbol{u} = \boldsymbol{u}_D & \text{on } \Gamma_D, \\ \mathbf{N}^T(\mathbf{D}\boldsymbol{\nabla}_{\mathtt{s}}\boldsymbol{u} - \mathbf{E}p) = \boldsymbol{t} & \text{on } \Gamma_N, \end{cases} \tag{2.2.7}$$

In this form, one can notice that the strongly enforced symmetry of the stress tensor gives the real traction force while the velocity-pressure formulation usually impose pseudo-traction which only account for the gradient of the velocity field instead of its symmetric part [10].

2.3 The FCFV framework

As explained in the introduction, the FCFV method is in essence a lowest order HDG method. Firstly, the strong form of the Stokes problem is proposed in the broken domain and a mixed variable is introduced. Secondly, the mixed problem is separated into the local and global ones. Then the integral forms of the FCFV local and global problems are derived using a constant degree of approximatios for all the variables.

2.3.1 FCFV strong forms

The domain Ω is partitioned in $\mathtt{n_{el}}$ disjoint subdomains Ω_e. The set of internal faces Γ is defined as

$$\Gamma := \left[\bigcup_{e=1}^{\mathtt{n_{el}}} \partial\Omega_e\right] \setminus \partial\Omega \tag{2.3.1}$$

In the proposed FCFV method, we introduce a mixed formulation to solve over broken domain the system of 1st order equations. Equation (2.2.7) can be rewritten on the broken

domain and in mixed form as:

$$\begin{cases} \boldsymbol{L} + \mathbf{D}^{1/2}\boldsymbol{\nabla}_{\mathtt{S}}\boldsymbol{u} = \mathbf{0} & \text{in } \Omega_e, \text{ and for } e = 1, \dots, \mathtt{n_{el}}, \\ \boldsymbol{\nabla}_{\mathtt{S}}^T\big(\mathbf{D}^{1/2}\boldsymbol{L} + \mathbf{E}p\big) = \boldsymbol{s} & \text{in } \Omega_e, \text{ and for } e = 1, \dots, \mathtt{n_{el}}, \\ \mathbf{E}^T\boldsymbol{\nabla}_{\mathtt{S}}\boldsymbol{u} = 0 & \text{in } \Omega_e, \text{ and for } e = 1, \dots, \mathtt{n_{el}}, \\ \boldsymbol{u} = \boldsymbol{u}_D & \text{on } \Gamma_D, \\ \mathbf{N}^T\big(\mathbf{D}^{1/2}\boldsymbol{L} + \mathbf{E}p\big) = -\boldsymbol{t} & \text{on } \Gamma_N, \\ [\![\boldsymbol{u} \otimes \boldsymbol{n}]\!] = \mathbf{0} & \text{on } \Gamma, \\ [\![\mathbf{N}^T\big(\mathbf{D}^{1/2}\boldsymbol{L} + \mathbf{E}p\big)]\!] = \mathbf{0} & \text{on } \Gamma, \end{cases} \tag{2.3.2}$$

where $\boldsymbol{L}$ is the so-called mixed variable representing the strain tensor. The last two equations are the *transmission conditions* enforcing the continuity of respectively the velocity and the flux across the interface Γ, where the *jump* operator $[\![\odot]\!]$ is defined along each portion of the interface as the sum of the values from the element on the right and the left, namely Ω_e and Ω_l [34],

$$[\![\odot]\!] = \odot_e + \odot_l. \tag{2.3.3}$$

Remark 1 In case of a purely Dirichlet problem(i.e. $\Gamma_N = \emptyset$), we need to add one more constrain to avoid indeterminacy of the pressure. A common choice relies on imposing zero mean value of the pressure on the whole domain, see e.g. [35, 36]:

$$\frac{1}{|\Omega|}\int_{\Omega} p d\Omega = 0 \tag{2.3.4}$$

Starting from the mixed formulation on the broken computational domain, the problem can be solved in two stages.

First, a set of $\mathtt{n_{el}}$ local problems is introduced to define $(\boldsymbol{L}_e, \boldsymbol{u}_e, p_e)$ element-by-element in terms of a novel independent variable $\hat{\boldsymbol{u}}$, namely

$$\begin{cases} \boldsymbol{L}_e + \mathbf{D}^{1/2}\boldsymbol{\nabla}_{\mathtt{S}}\boldsymbol{u}_e = \mathbf{0} & \text{in } \Omega_e \\ \boldsymbol{\nabla}_{\mathtt{S}}^T\big(\mathbf{D}^{1/2}\boldsymbol{L}_e + \mathbf{E}p_e\big) = \boldsymbol{s} & \text{in } \Omega_e \\ \mathbf{E}^T\boldsymbol{\nabla}_{\mathtt{S}}\boldsymbol{u}_e = 0 & \text{in } \Omega_e \\ \boldsymbol{u}_e = \boldsymbol{u}_D & \text{on } \partial\Omega_e \cap \Gamma_D, \\ \boldsymbol{u}_e = \hat{\boldsymbol{u}} & \text{on } \partial\Omega_e \setminus \Gamma_D, \end{cases} \tag{2.3.5}$$

where $\hat{\boldsymbol{u}}$ represents the trace of the velocity on the mesh skeleton $\Gamma \cup \Gamma_N$. Remark that Equation (2.3.5) is a purely Dirichlet boundary value problem. An additional constraint has to be added to remove the indeterminacy of the pressure, namely

$$\frac{1}{|\partial\Omega_e|}\int_{\partial\Omega_e} \mathrm{p}_e d\Gamma = \rho_e \tag{2.3.6}$$

where ρ_e denotes the mean pressure on the boundary of the element Ω_e.

Similarly, the global problem in Voigt notation is

$$\begin{cases} [\![\boldsymbol{u} \otimes \boldsymbol{n}]\!] = \mathbf{0} & \text{on } \Gamma, \\ [\![\mathbf{N}^T(\mathbf{D}^{1/2}\boldsymbol{L} + \mathbf{E}\,p)]\!] = \mathbf{0} & \text{on } \Gamma, \\ \mathbf{N}^T(\mathbf{D}^{1/2}\boldsymbol{L} + \mathbf{E}\,p) = -\boldsymbol{t} & \text{on } \Gamma_N, \end{cases} \tag{2.3.7}$$

As the continuity of $\boldsymbol{u}$ is already guaranteed by the uniqueness of $\hat{\boldsymbol{u}}$ for each point of Γ, the jump of $\boldsymbol{u}$ in Equation (2.3.7) is automatically satisfied. Therefore, the transmission conditions are simply

$$\begin{cases} [\![\mathbf{N}^T(\mathbf{D}^{1/2}\boldsymbol{L} + \mathbf{E}\,p)]\!] = \mathbf{0} & \text{on } \Gamma, \\ \mathbf{N}^T(\mathbf{D}^{1/2}\boldsymbol{L} + \mathbf{E}\,p) = -\boldsymbol{t} & \text{on } \Gamma_N, \end{cases} \tag{2.3.8}$$

The compatibility condition imposing the weak incompressibility constraint element by element is used to close the global problem

$$\int_{\partial\Omega_e \setminus \Gamma_D} \mathbf{E}^T \mathbf{N}_e \hat{\boldsymbol{u}} d\Gamma + \int_{\partial\Omega_e \cap \Gamma_D} \mathbf{E}^T \mathbf{N}_e \boldsymbol{u}_D d\Gamma = 0 \tag{2.3.9}$$

2.3.2 FCFV integral forms

For each cell $e = 1, \ldots, \mathtt{n_{el}}$, we calculate the integral form of the problem by applying the divergence theorem. The local problems reads as

$$\begin{aligned} &\int_{\Omega_e} \boldsymbol{L}_e^h d\Omega + \int_{\partial\Omega_e} \mathbf{N}_e^T \mathbf{D}^{1/2} \boldsymbol{u}_e^h d\Gamma = \mathbf{0} \\ &\int_{\partial\Omega_e} \mathbf{N}_e^T \widehat{(\mathbf{D}^{1/2}\boldsymbol{L}_e^h + \mathbf{E}p_e^h)} d\Gamma = \int_{\Omega_e} \boldsymbol{s} d\Omega \\ &\int_{\partial\Omega_e \setminus \Gamma_D} \mathbf{E}^T \mathbf{N}_e \hat{\boldsymbol{u}} d\Gamma + \int_{\partial\Omega_e \cap \Gamma_D} \mathbf{E}^T \mathbf{N}_e \boldsymbol{u}_D d\Gamma = 0 \\ &\frac{1}{|\partial\Omega_e|} \int_{\partial\Omega_e} \mathrm{p}_e d\Gamma = \rho_e \end{aligned} \tag{2.3.10}$$

where the trace of the numerical flux is defined as follows

$$\mathbf{N}_e^T \widehat{\left(\mathbf{D}^{1/2}\boldsymbol{L}_e^h + \mathbf{E}\,p_e^h\right)} := \begin{cases} \mathbf{N}_e^T\left(\mathbf{D}^{1/2}\boldsymbol{L}_e^h + \mathbf{E}\,p_e^h\right) + \tau^d(\boldsymbol{u}_e^h - \boldsymbol{u}_D) & \text{on } \partial\Omega_e \cap \Gamma_D, \\ \mathbf{N}_e^T\left(\mathbf{D}^{1/2}\boldsymbol{L}_e^h + \mathbf{E}\,p_e^h\right) + \tau^d(\boldsymbol{u}_e^h - \hat{\boldsymbol{u}}^h) & \text{elsewhere.} \end{cases} \tag{2.3.11}$$

The stabilisation parameter τ^d is defined as $\tau^d = \kappa\frac{\nu}{l}$, where κ is the scaling factor, l is a characteristic length of the domain. It is uniform everywhere and appropriate κ is chosen from the sensitivity study. The stabilisation parameter plays a crucial role in the stability, accuracy and convergence properties of the resulting FCFV method [37].

It needs to be mentioned that the third equation in (2.3.10) which describes the incompressibility of the flow is simply a function of $\hat{\boldsymbol{u}}$ and $\boldsymbol{u}_D$ after introducing integration by parts. Therefore, it will be moved to the global problem, see Equation (2.3.9).

By plugging Equation (2.3.11) into Equation (2.3.10) and introducing the Dirichlet boundary conditions of the local problem we have

$$\begin{aligned}
&\int_{\Omega_e} \boldsymbol{L}_e^h d\Omega + \int_{\partial\Omega_e\cap\Gamma_D} \mathbf{N}_e^T \mathbf{D}^{1/2} \boldsymbol{u}_D d\Gamma + \int_{\partial\Omega_e\setminus\Gamma_D} \mathbf{N}_e^T \mathbf{D}^{1/2} \hat{\boldsymbol{u}}^h d\Gamma = \mathbf{0} \\
&\int_{\partial\Omega_e} \mathbf{N}_e^T (\mathbf{D}^{1/2} \boldsymbol{L}_e^h + \mathbf{E} p_e^h) d\Gamma + \int_{\partial\Omega_e} \tau^d \boldsymbol{u}_e^h d\Gamma = \int_{\Omega_e} \boldsymbol{s} d\Omega + \int_{\partial\Omega_e\cap\Gamma_D} \tau^d \boldsymbol{u}_D d\Gamma + \int_{\partial\Omega_e\setminus\Gamma_D} \tau^d \hat{\boldsymbol{u}}^h d\Gamma \\
&\frac{1}{|\partial\Omega_e|} \int_{\partial\Omega_e} \mathrm{p}_e d\Gamma = \rho_e
\end{aligned} \tag{2.3.12}$$

Applying the divergence theorem in the momentum equation in Equation (2.3.12) again, we have

$$\begin{aligned}
&\int_{\Omega_e} \boldsymbol{L}_e^h d\Omega + \int_{\partial\Omega_e\cap\Gamma_D} \mathbf{N}_e^T \mathbf{D}^{1/2} \boldsymbol{u}_D d\Gamma + \int_{\partial\Omega_e\setminus\Gamma_D} \mathbf{N}_e^T \mathbf{D}^{1/2} \hat{\boldsymbol{u}}^h d\Gamma = \mathbf{0} \\
&\int_{\Omega_e} (\boldsymbol{\nabla}_{\mathbf{S}}^T \mathbf{D}^{1/2} \boldsymbol{L}_e^h + \boldsymbol{\nabla}_{\mathbf{S}}^T \mathbf{E} p_e^h) d\Omega + \int_{\partial\Omega_e} \tau^d \boldsymbol{u}_e^h d\Gamma = \int_{\Omega_e} \boldsymbol{s} d\Omega + \int_{\partial\Omega_e\cap\Gamma_D} \tau^d \boldsymbol{u}_D d\Gamma + \int_{\partial\Omega_e\setminus\Gamma_D} \tau^d \hat{\boldsymbol{u}}^h d\Gamma \\
&\frac{1}{|\partial\Omega_e|} \int_{\partial\Omega_e} \mathrm{p}_e d\Gamma = \rho_e
\end{aligned} \tag{2.3.13}$$

Analogously, the integral form of the global problem can be written as

$$\sum_{e=1}^{\mathtt{n_{el}}} \Big\{ \int_{\partial\Omega_e\cap\Gamma} \mathbf{N}_e^T (\widehat{\mathbf{D}^{1/2} \boldsymbol{L}_e^h + \mathbf{E} p_e^h}) d\Gamma + \int_{\partial\Omega_e\cap\Gamma_N} \mathbf{N}_e^T (\widehat{\mathbf{D}^{1/2} \boldsymbol{L}_e^h + \mathbf{E} p_e^h}) + \boldsymbol{t} d\Gamma \Big\} = \mathbf{0} \tag{2.3.14}$$

Plugging (2.3.11) into Equation (2.3.14), the integral global form reads as

$$\begin{aligned}
\sum_{e=1}^{\mathtt{n_{el}}} \Big\{ \int_{\partial\Omega_e\setminus\Gamma_D} (\mathbf{N}_e^T \mathbf{D}^{1/2} \boldsymbol{L}_e^h + \mathbf{N}_e^T \mathbf{E} p_e^h) d\Gamma + \int_{\partial\Omega_e\setminus\Gamma_D} \tau^d \boldsymbol{u}_e^h d\Gamma - \int_{\partial\Omega_e\setminus\Gamma_D} \tau^d \hat{\boldsymbol{u}}^h d\Gamma \Big\} \\
= - \sum_{e=1}^{\mathtt{n_{el}}} \int_{\partial\Omega_e\cap\Gamma_N} \boldsymbol{t} d\Gamma
\end{aligned} \tag{2.3.15}$$

As discussed before, the compatibility condition is included in the global form to close the problem

$$\int_{\partial\Omega_e\setminus\Gamma_D} \mathbf{E}^T \mathbf{N}_e \hat{\boldsymbol{u}} d\Gamma + \int_{\partial\Omega_e\cap\Gamma_D} \mathbf{E}^T \mathbf{N}_e \boldsymbol{u}_D d\Gamma = 0 \quad \text{for } e = 1, \ldots, \mathtt{n_{el}}$$

2.3.3 FCFV linear system

For the sake of readability, henceforth the superscript h is omitted in the derivation of the linear system. Moreover, we introduce the following notation for the sets of faces

$$\mathcal{A}_e := 1, \dots, \mathtt{n_{fc}} \tag{2.3.16}$$
$$\mathcal{D}_e := \{j \in \mathcal{A}_e | \Gamma_{e,j} \cap \Gamma_D \neq \emptyset\} \tag{2.3.17}$$
$$\mathcal{N}_e := \{j \in \mathcal{A}_e | \Gamma_{e,j} \cap \Gamma_N \neq \emptyset\} \tag{2.3.18}$$
$$\mathcal{B}_e := \mathcal{A}_e \setminus \mathcal{D}_e = \{j \in \mathcal{A}_e | \Gamma_{e,j} \cap \Gamma_D = \emptyset\} \tag{2.3.19}$$
$$\mathcal{I}_e := \{j \in \mathcal{A}_e | \Gamma_{e,j} \cap \partial\Omega = \emptyset\} \tag{2.3.20}$$
$$\tag{2.3.21}$$

where $\mathcal{A}_e$ is the set of indices for all the faces of element Ω_e, $\mathcal{D}_e$ is the set of indices for all the faces of element Ω_e on the Dirichlet boundary, $\mathcal{N}_e$ is the set of indices for all the faces of element Ω_e on the Neumann boundary, $\mathcal{B}_e$ is the set of indices for all the faces of element Ω_e not on the Dirichlet boundary, $\mathcal{I}_e$ is the set of indices for all the faces of element Ω_e not on the boundary.

With a degree of approximation $k = 0$ in each element for both $\boldsymbol{L}_e$,$\boldsymbol{u}_e$,p_e and also a degree of approximation $k = 0$ in each face/edge for $\hat{\mathbf{u}}$, the integral form of the local problem leads to

$$-|\Omega_e|\mathbf{L}_e = \sum_{j\in\mathcal{D}_e} |\boldsymbol{\Gamma}_{e,j}|\mathbf{D}^{1/2}\mathbf{N}_{e,j}\boldsymbol{u}_{D,j} + \sum_{j\in\mathcal{B}_e} |\boldsymbol{\Gamma}_{e,j}|\mathbf{D}^{1/2}\mathbf{N}_{e,j}\hat{\mathbf{u}}_j \tag{2.3.22a}$$
$$\sum_{j\in\mathcal{A}_e} |\boldsymbol{\Gamma}_{e,j}|\tau_j^d\mathbf{u}_e = |\Omega_e|\boldsymbol{s}_e + \sum_{j\in\mathcal{D}_e} |\boldsymbol{\Gamma}_{e,j}|\tau_j^d\boldsymbol{u}_{D,j} + \sum_{j\in\mathcal{B}_e} |\boldsymbol{\Gamma}_{e,j}|\tau_j^d\hat{\mathbf{u}}_j \tag{2.3.22b}$$
$$\mathrm{p}_e = \rho_e \tag{2.3.22c}$$

Benefiting from the constant degree of approximation, the two equations of the local problem decouple and it is possible to obtain a closed form expression for $\boldsymbol{L}_e$, $\boldsymbol{u}_e$ and p_e as a function of $\hat{\boldsymbol{u}}$ and ρ_e namely

$$\mathbf{L}_e = -|\Omega_e|^{-1}\boldsymbol{z}_e - |\Omega_e|^{-1}\sum_{j\in\mathcal{B}_e} |\boldsymbol{\Gamma}_{e,j}|\mathbf{D}^{1/2}\mathbf{N}_{e,j}\hat{\mathbf{u}}_j \tag{2.3.23a}$$
$$\mathbf{u}_e = \alpha_e^{-1}\boldsymbol{\beta}_e + \alpha_e^{-1}\sum_{j\in\mathcal{B}_e} |\boldsymbol{\Gamma}_{e,j}|\tau_j^d\hat{\boldsymbol{u}}_j \tag{2.3.23b}$$
$$\mathrm{p}_e = \rho_e \tag{2.3.23c}$$

where

$$\alpha_e := \sum_{j\in\mathcal{A}_e} |\boldsymbol{\Gamma}_{e,j}|\tau_j^d \tag{2.3.24a}$$
$$\boldsymbol{\beta}_e := |\Omega_e|\boldsymbol{s}_e + \sum_{j\in\mathcal{D}_e} |\boldsymbol{\Gamma}_{e,j}|\tau_j^d\boldsymbol{u}_{D,j} \tag{2.3.24b}$$

$$\boldsymbol{z}_e := \sum_{j\in\mathcal{D}_e} |\boldsymbol{\Gamma}_{e,j}|\mathbf{D}^{1/2}\mathbf{N}_{e,j}\boldsymbol{u}_{D,j} \tag{2.3.24c}$$

Similarly, with a degree of approximation $k = 0$ in the global equations, we have

$$\begin{aligned}\sum_{e=1}^{\mathtt{n_{el}}}\Big\{|\boldsymbol{\Gamma}_{e,i}|\mathbf{N}_{e,i}^T\mathbf{D}^{1/2}\mathbf{L}_e+|\boldsymbol{\Gamma}_{e,i}|\mathbf{E}^T\mathbf{N}_{e,i}\,\mathrm{p}_e+|\boldsymbol{\Gamma}_{e,i}|\tau_i^d\,\mathrm{u}_e-|\boldsymbol{\Gamma}_{e,i}|\tau_i^d\,\hat{\mathbf{u}}_i\Big\}\\ = -\sum_{e=1}^{\mathtt{n_{el}}}|\boldsymbol{\Gamma}_{e,i}|\boldsymbol{t}_i\mathcal{X}_{\mathcal{N}e}(i)\ \text{ for } i\in\mathcal{B}_e,\end{aligned} \tag{2.3.25a}$$

$$\sum_{j\in\mathcal{B}_e}|\boldsymbol{\Gamma}_{e,j}|\mathbf{E}^T\mathbf{N}_{e,i}\hat{\mathbf{u}} = -\sum_{j\in\mathcal{D}_e}|\boldsymbol{\Gamma}_{e,j}|\mathbf{E}^T\mathbf{N}_{e,j}\boldsymbol{u}_{D,j}\ \text{ for } e=1,\ldots,\mathtt{n_{el}}\ , \tag{2.3.25b}$$

where $\mathcal{X}_{\mathcal{N}e}$ is the indicator function of the set $\mathcal{N}_e$, i.e.

$$\mathcal{X}_{\mathcal{N}e}(i) = \begin{cases}1 & \text{if}\quad i\in\mathcal{N}_e\\ 0 & \text{otherwise}\end{cases} \tag{2.3.26}$$

After introducing the closed form expressions of the mixed and primal variable of Equation(2.3.23a) and Equation(2.3.23b), a linear system of equations is obtained

$$\begin{aligned}\sum_{e=1}^{\mathtt{n_{el}}}\Big\{|\boldsymbol{\Gamma}_{e,i}|\mathbf{N}_{e,i}^T\mathbf{D}^{1/2}(-|\Omega_e|^{-1}\boldsymbol{z}_e-|\Omega_e|^{-1}|\boldsymbol{\Gamma}_{e,j}|\mathbf{N}_{e,j}^T\mathbf{D}^{1/2}\hat{\mathbf{u}}_i)+|\boldsymbol{\Gamma}_{e,i}|\mathbf{E}^T\mathbf{N}_{e,i}\,\mathrm{p}_e\\ +|\boldsymbol{\Gamma}_{e,i}|\tau_i^d\,(\alpha_e^{-1}\boldsymbol{\beta}_e+\alpha_e^{-1}|\boldsymbol{\Gamma}_{e,j}|\tau_j^d\hat{\mathbf{u}}_j)-|\boldsymbol{\Gamma}_{e,i}|\tau_i^d\,\hat{\mathbf{u}}_i\Big\} = -\sum_{e=1}^{\mathtt{n_{el}}}|\boldsymbol{\Gamma}_{e,i}|\boldsymbol{t}_i\mathcal{X}_{\mathcal{N}e}(i)\ \text{ for } i,j\in\mathcal{B}_e,\end{aligned} \tag{2.3.27a}$$

$$\sum_{j\in\mathcal{B}_e}|\boldsymbol{\Gamma}_{e,j}|\mathbf{E}^T\mathbf{N}_{e,j}\hat{\mathbf{u}}_j = -\sum_{j\in\mathcal{D}_e}|\boldsymbol{\Gamma}_{e,j}|\mathbf{E}^T\mathbf{N}_{e,j}\boldsymbol{u}_{D,j}\ \text{ for } e=1,\ldots,\mathtt{n_{el}}\ , \tag{2.3.27b}$$

The global problem can be written in terms of the global unknowns $\hat{\boldsymbol{u}}$ and ρ. The following linear system is obtained:

$$\begin{bmatrix}\hat{\mathbf{K}}_{\hat{u}\hat{u}} & \hat{\mathbf{K}}_{\hat{u}\rho}\\ \hat{\mathbf{K}}_{\hat{u}\rho}^T & \mathbf{0}_{\mathtt{n_{el}}}\end{bmatrix}\begin{Bmatrix}\hat{\mathbf{u}}\\ \boldsymbol{\rho}\end{Bmatrix} = \begin{Bmatrix}\hat{\mathbf{f}}_{\hat{u}}\\ \hat{\mathbf{f}}_{\rho}\end{Bmatrix} \tag{2.3.28}$$

$$(\hat{\mathbf{K}}_{\hat{u}\hat{u}})_{i,j}^e := |\boldsymbol{\Gamma}_{e,i}|(|\boldsymbol{\Gamma}_{e,j}|\alpha_e^{-1}\tau_i^d\tau_j^d\boldsymbol{I}_{\mathtt{n_{sd}}}-|\boldsymbol{\Gamma}_{e,j}||\Omega_e|^{-1}\mathbf{N}_{e,i}^T\mathbf{D}^{1/2}\mathbf{D}^{1/2}\mathbf{N}_{e,j}-\tau_i^d\delta_{ij}\boldsymbol{I}_{\mathtt{n_{sd}}}) \tag{2.3.29a}$$

$$(\hat{\mathbf{K}}_{\hat{u}\rho})_i^e := |\boldsymbol{\Gamma}_{e,i}|\mathbf{E}^T\mathbf{N}_{e,i} \tag{2.3.29b}$$

$$(\hat{\mathbf{f}}_{\hat{u}})_i^e := |\boldsymbol{\Gamma}_{e,i}|(-\tau_i^d\,\alpha_e^{-1}\boldsymbol{\beta}_e+|\Omega_e|^{-1}\mathbf{N}_{e,i}^T\mathbf{D}^{1/2}\boldsymbol{z}_e-\boldsymbol{t}_i\mathcal{X}_{\mathcal{N}e}(i)) \tag{2.3.29c}$$

$$(\hat{\mathbf{f}}_{\rho})^e := -\sum_{j\in\mathcal{D}_e}|\boldsymbol{\Gamma}_{e,j}|\mathbf{E}^T\mathbf{N}_{e,i}\boldsymbol{u}_{D,j} \tag{2.3.29d}$$

for $i,j\in\mathcal{B}_e$.

Remark 2 As aforementioned, if all Dirichlet boundaries are applied (i.e., $\Gamma_N = \emptyset$), we impose zero mean value of the pressure on the whole domain to avoid the indeterminancy of the pressure:

$$\sum_{e=1}^{\mathtt{n_{el}}} |\Omega_e| \rho_e = 0. \tag{2.3.30}$$

In this case, an additional equation will be added to the global system of Equation (2.3.28) by means of a Lagrange multiplier, which acts as the extra constraint on the pressure.

2.4 Numerical studies

In this section, two examples are utilized to verify accuracy and the convergence rate of the FCFV method for Stokes equations – one is the rotating flow and the other is the modified Wang flow. First, simulations are carried out under difference mesh sizes and the numerical results are qualatitively compared with the analytical solution. Second, the convergence rate of the $\mathcal{L}_2$ error of primal and mixed variables is analyzed. At last, the influence of the stabilisation parameter on the accuracy of the results is studied.

2.4.1 Optimal convergence rate of the primal and mixed variables

Two kinds of structured meshes are considered in the numerical studies, which are illustrated in Figure 2.1. The triangular mesh is constructed by dividing each cell in the quadrilateral mesh into four parts. The characteristic cell size is $h = 2^{-r}$ where r denotes the level of mesh refinement.

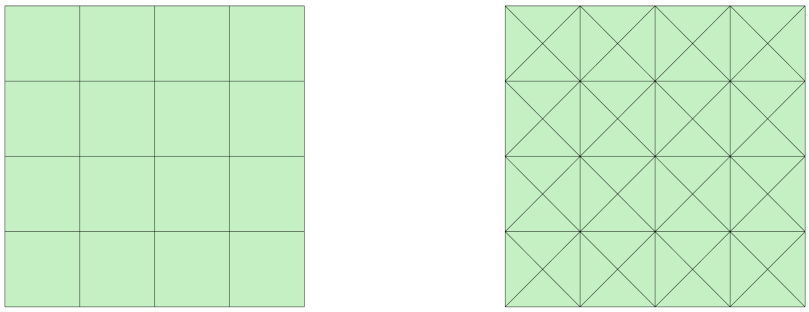

(a) Quadrilateral mesh (b) Triangular mesh

Figure 2.1: Second level of refinement for two types of mesh

Rotating flow

The first example of a two dimensional synthetic problem is taken from [10] and is considered in the domain $\Omega = [0, 1]^2$. It is the analytical solution of stationary Stokes flow where the fluid viscosity is taken as $\nu = 1$. The boundary $\partial\Omega$ is split into two disjoint parts, namely $\Gamma_N = \{(x, y) \in \mathbb{R}^2 | y = 0\}$ where a traction $\boldsymbol{t}$ is imposed and $\Gamma_D = \partial\Omega \backslash \Gamma_N$ where a velocity profile $\boldsymbol{u}_D$ is set. The source term $\boldsymbol{s}$ and the boundary data $\boldsymbol{t}$ are chosen such

that the analytical solution is

$$\begin{cases} u_1(x,y) = x^2(1-x)^2(2y - 6y^2 + 4y^3), \\ u_2(x,y) = -y^2(1-y)^2(2x - 6x^2 + 4x^2), \\ p(x,y) = x(1-x) \end{cases} \tag{2.4.1}$$

where u_1 and u_2 are the two components of the velocity field vector $\boldsymbol{u}$.

The feature of the rotating flow can be observed in Figure 2.2, which illustrates that the velocity vectors rotate around the center of the domain. The analytical solution of velocity and pressure fields are shown in Figure 2.3 for comparison with the numerical ones.

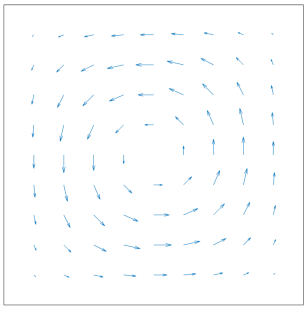

Figure 2.2: Analytical velocity vectors

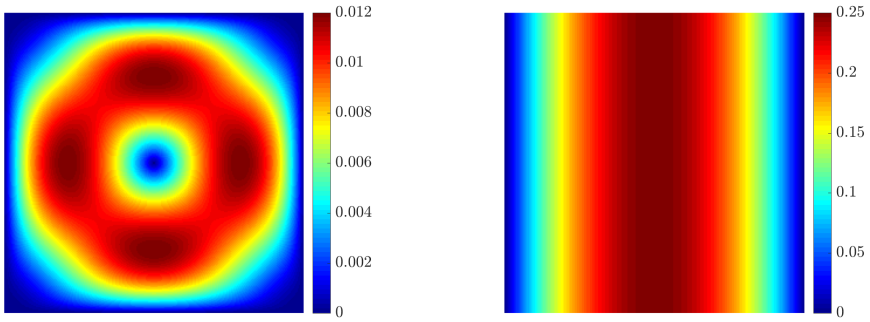

(a) $\|\boldsymbol{u}\|_2$ (b) p

Figure 2.3: Analytical velocity and pressure fields

The numerical results calculated with the different levels of mesh refinements are illustrated in Figure 2.4 and Figure 2.5. The stabilisation parameter at each face is chosen as a constant value $\tau^d = 10\frac{\nu}{l}$. Compared with Figure 2.3, the increase in accuracy of the velocity and pressure fields can be observed as the mesh is refined. Moreover, triangular meshes

perform better than the quadrilateral ones because, for a given level of mesh refinements, they feature a higher number of degrees of freedom with respect to the corresponding quadrilateral ones.

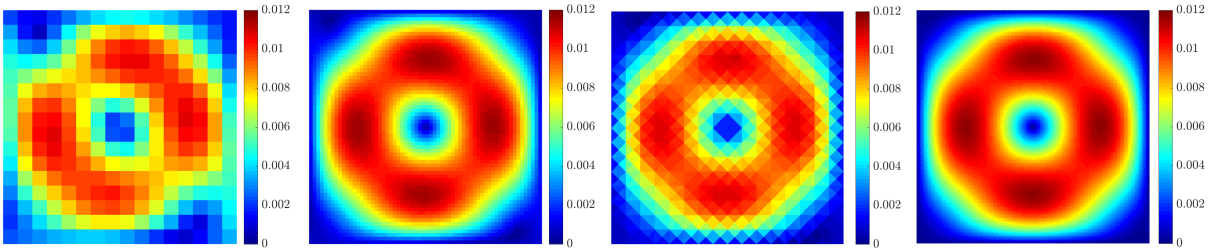

(a) QUA H4 (b) QUA H6 (c) TRI H4 (d) TRI H6

Figure 2.4: Numerical approximation of the module of velocity (QUA: quadrilateral mesh, TRI: triangular mesh; H4: fourth level refinement, H6: sixth level refinement)

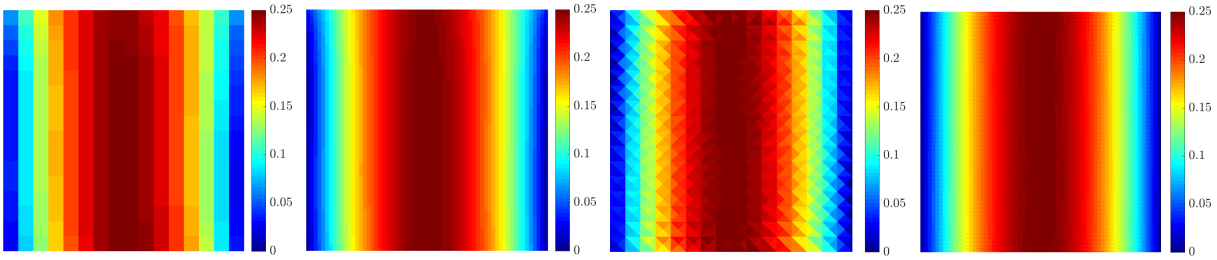

(a) QUA H4 (b) QUA H6 (c) TRI H4 (d) TRI H6

Figure 2.5: Numerical approximation of the pressure field (QUA: quadrilateral mesh, TRI: triangular mesh; H4: fourth level refinement, H6: sixth level refinement)

The optimal convergence rate is studied with the $\mathcal{L}_2(\Omega)$ norm of the error, which is defined as

$$\|E_\omega\|_{\mathcal{L}_2(\Omega)} = \left\{ \frac{\int_\Omega (\omega^h - \omega) \cdot (\omega^h - \omega) d\Omega}{\int_\Omega \omega \cdot \omega d\Omega} \right\}^{1/2} \tag{2.4.2}$$

where ω is the exact solution and ω^h is the numerical approximation. In this problem, ω can be $\boldsymbol{u}$, $\boldsymbol{L}$ and p.

Figure 2.6 shows the convergence rate of the error of the primal and mixed variables measured in the $\mathcal{L}_2(\Omega)$ norm as a function of the characteristic element size with both quadrilateral and triangular meshes. It can be observed that optimal first-order convergence rate is achieved for the velocity, strain tensor and pressure.

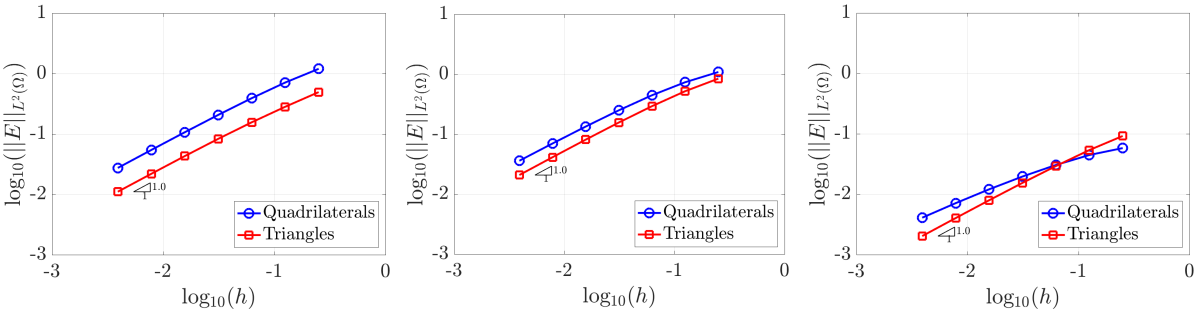

(a) $\boldsymbol{u}$ (b) $\boldsymbol{L}$ (c) p

Figure 2.6: Convergence rate of rotating flow

Modified Wang flow

The second example is a modified Wang flow. The pressure is redefined to be $p = x(1-x)$. The boundary $\partial\Omega$ is also split into two disjoint parts, namely $\Gamma_N = \{(x, y) \in \mathbb{R}^2 | y = 0\}$ where a traction $\boldsymbol{t}$ is imposed and $\Gamma_D = \partial\Omega \backslash \Gamma_N$ where a velocity profile $\boldsymbol{u}_D$ is set. The viscosity parameter is set to $\nu = 1$ and the source term $\boldsymbol{s}$ and the boundary data $\boldsymbol{t}$ are chosen such that the analytical solution is

$$\begin{cases} u_1(x, y) = 2y - \lambda \exp(-\lambda y) \cos(\lambda x), \\ u_2(x, y) = \lambda \exp(-\lambda y) \sin(\lambda x), \\ p(x, y) = x(1 - x); \end{cases} \tag{2.4.3}$$

The analytical solution of velocity and pressure fields are shown in Figure 2.7.

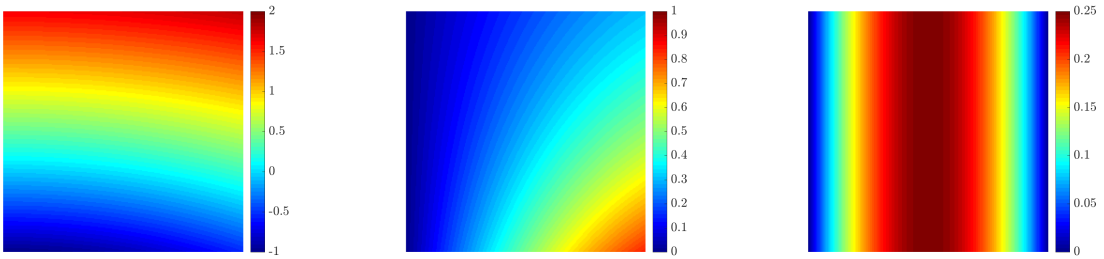

(a) u_1 (b) u_2 (c) p

Figure 2.7: Analytical velocity and pressure fields

The numerical results calculated with the sixth and ninth level meshes are illustrated in Figure 2.8 and 2.9. In this case, the stabilisation parameter is also set to be $\tau^d = 10\frac{\nu}{l}$. Same as what has been observed in the rotating flow, the refinement of the mesh gives an

increase in the accuracy of the result. In this case, reasonable velocity plots can be obtained with sixth level mesh while the discrepancy of the pressure field is relatively large. If we refine the mesh to the ninth level, an accurate pressure field can be obtained. Usually, the accuracy of pressure is more difficult to achieve than that of velocity. We might need a very fine mesh in order to guarantee an acceptable error in the pressure field.

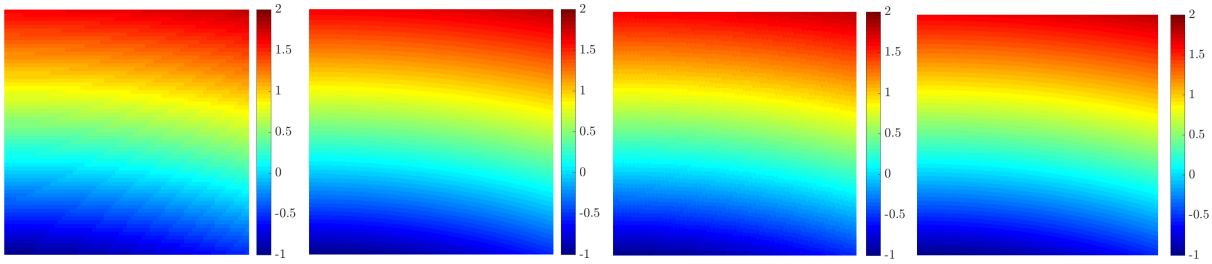

(a) QUA H6 (b) QUA H9 (c) TRI H6 (d) TRI H9

Figure 2.8: Numerical approximation of u_1 (QUA: quadrilateral mesh, TRI: triangular mesh; H6: sixth level refinement, H9: ninth level refinement)

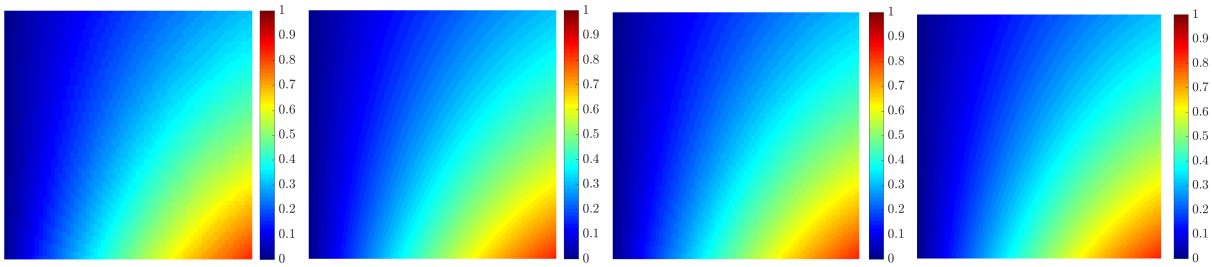

(a) QUA H6 (b) QUA H9 (c) TRI H6 (d) TRI H9

Figure 2.9: Numerical approximation of u_2 (QUA: quadrilateral mesh, TRI: triangular mesh; H6: sixth level refinement, H9: ninth level refinement)

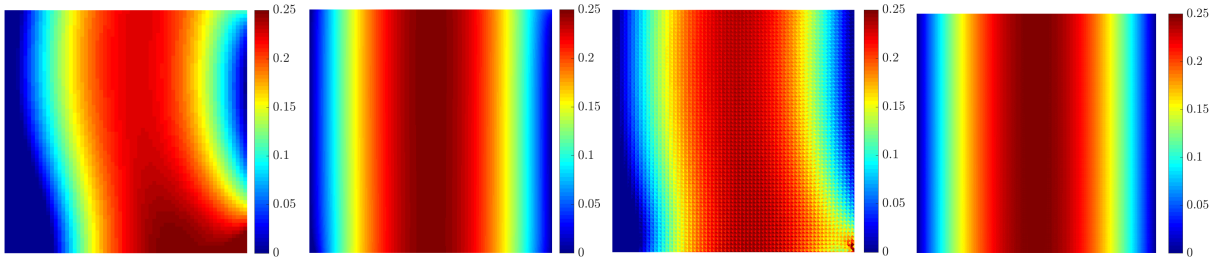

(a) QUA H6 (b) QUA H9 (c) TRI H6 (d) TRI H9

Figure 2.10: Numerical approximation of the pressure field (QUA: quadrilateral mesh, TRI: triangular mesh; H6: sixth level refinement, H9: ninth level refinement)

Same as the first example, the convergence rate is studied on the modified Wang flow with the boundary conditions as mentioned before. The stabilisation parameter is chosen to be $10\frac{\nu}{l}$ over the whole domain. It can be seen from Figure 2.11 that optimal convergence rates are achieved for both primal and mixed variables.

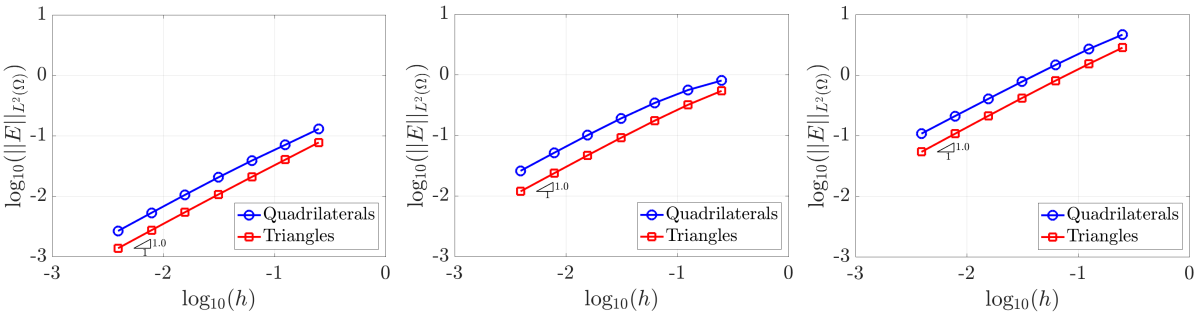

(a) $\boldsymbol{u}$ (b) $\boldsymbol{L}$ (c) p

Figure 2.11: Convergence rate of the modified Wang flow

2.4.2 Influence of the stabilisation parameter

As mentioned above, the stabilisation parameter plays an important role in the accuracy, stability and convergence rate of the method [26, 38, 39]. Therefore, further studies on the stabilisation parameter has been done for the Stokes problem.

Figure 2.12 shows the evolution of the $\mathcal{L}_2$ norm error of primal and mixed variables $\boldsymbol{u}$,p and $\boldsymbol{L}$ with respected to the stabilisation parameter τ^d for the mesh of the fourth and fifth level of refinement. It is tested by two examples above – Ex1: rotating flow, Ex2: modified Wang flow. For values of κ between 1 and 50 the error in all variables is acceptable. Thus, the choice $\kappa = 10$ is utilized above for the convergence study.

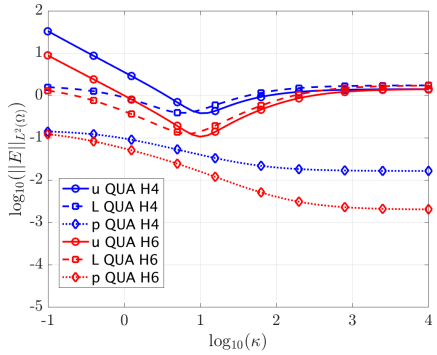

(a) Ex1 Quadrilateral mesh

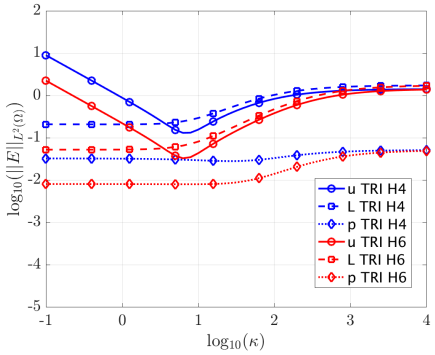

(b) Ex1 Triangular mesh

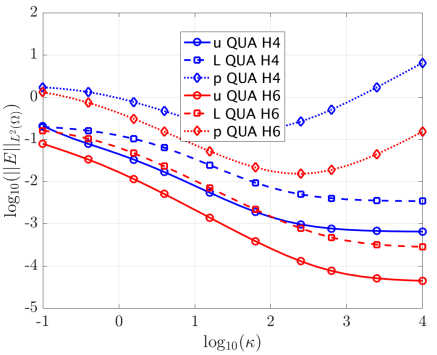

(c) Ex2 Quadrilateral mesh

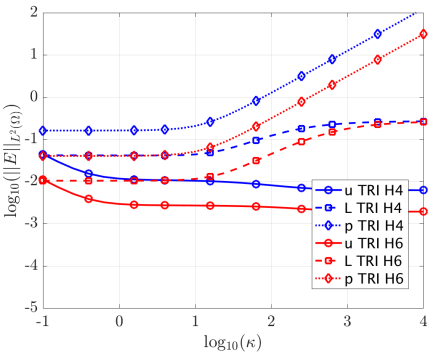

(d) Ex2 Triangular mesh

Figure 2.12: Error evolution of $\boldsymbol{u}$, p and $\boldsymbol{L}$ as a function of κ

Chapter 3

FCFV method for the Oseen equations

One of the main numerical difficulties of incompressible Navier-Stokes equations is the nonlinearity introduced by the convection term. In this chapter, a linearized version of the convection term is considered via the Oseen equations. Same as what we have done in the Stokes problem, the strong form is written using Voigt notations. Then the FCFV method is applied in order to derive the integral form and the linear system of equations. At last, one 2D example of the rotating flow from the analytical solution of the Navier-Stokes problem is analysed to validate the method. The optimal convergence rate is studied. Moreover, the influence of the different choices of advection stabilisation parameters and their magnitude are presented.

3.1 Governing equations

The Oseen equations are the linearized incompressible Navier-Stokes equations with a linear solenoidal convective field $\boldsymbol{a}$. The strong form is written as:

$$\begin{cases} -\boldsymbol{\nabla}\cdot(2\nu\boldsymbol{\nabla}^{\mathrm{s}}\boldsymbol{u}-p\boldsymbol{I}_{\mathtt{n_{sd}}})+\boldsymbol{\nabla}\cdot(\boldsymbol{u}\otimes\boldsymbol{a})=\boldsymbol{s} & \text{in } \Omega,\\ \boldsymbol{\nabla}\cdot\boldsymbol{u}=0 & \text{in } \Omega,\\ \boldsymbol{u}=\boldsymbol{u}_D & \text{on } \Gamma_D,\\ \boldsymbol{n}\cdot\big(2\nu\boldsymbol{\nabla}^{\mathrm{s}}\boldsymbol{u}-p\boldsymbol{I}_{\mathtt{n_{sd}}}\big)-(\boldsymbol{u}\otimes\boldsymbol{a})\boldsymbol{n}=\boldsymbol{t} & \text{on } \Gamma_N, \end{cases} \tag{3.1.1}$$

where $\boldsymbol{a}$ is a divergence-free convective field. If $\boldsymbol{a}\cdot\boldsymbol{n}=0$, a tension $\boldsymbol{t}$ is applied on the Neumann boundary, modelling a physical wall. Otherwise, an artificial condition is imposed on Γ_N which allows to model outflow boundaries for internal flows. In this project, $\boldsymbol{a}$ is defined as the analytical solution of the velocity. The only difference between the Stokes equations and the Oseen equations is the introduction of the linear convection term.

3.2 The FCFV framework

The derivation of the FCFV formulations of the Oseen equations is similar to what we have done for the Stokes problem. Firstly, we write the strong form of the local and global problem using Voigt notations. Second, we apply divergence theorem to derive the integral forms. Then by assuming constant approximation in each element, the linear system of equations is obtained.

3.2.1 FCFV strong forms

We can rewrite Equation (3.1.1) into the Voigt form by adding the convection term to the Voigt form of the Stokes equations

$$\begin{cases} -\boldsymbol{\nabla}_{\mathtt{s}}^T(\mathbf{D}\boldsymbol{\nabla}_{\mathtt{s}}\boldsymbol{u} - \mathbf{E}p) + \boldsymbol{\nabla}(\boldsymbol{u}\otimes\boldsymbol{a}) = \boldsymbol{s} & \text{in } \Omega, \\ \mathbf{E}^T\boldsymbol{\nabla}_{\mathtt{s}}\boldsymbol{u} = 0 & \text{in } \Omega, \\ \boldsymbol{u} = \boldsymbol{u}_D & \text{on } \Gamma_D, \\ \mathbf{N}^T(\mathbf{D}\boldsymbol{\nabla}_{\mathtt{s}}\boldsymbol{u} - \mathbf{E}p) - (\boldsymbol{u}\otimes\boldsymbol{a})\boldsymbol{n} = \boldsymbol{t} & \text{on } \Gamma_N, \end{cases} \tag{3.2.1}$$

Equation (3.2.1) can be rewritten on the broken domain and in mixed form as

$$\begin{cases} \boldsymbol{L} + \mathbf{D}^{1/2}\boldsymbol{\nabla}_{\mathtt{s}}\boldsymbol{u} = \mathbf{0} & \text{in } \Omega_e, \text{ and for } e = 1,\dots,\mathtt{n_{el}}, \\ \boldsymbol{\nabla}_{\mathtt{s}}^T\mathbf{D}^{1/2}\boldsymbol{L} + \boldsymbol{\nabla}_{\mathtt{s}}^T\mathbf{E}p + \boldsymbol{\nabla}\cdot(\boldsymbol{u}\otimes\boldsymbol{a}) = \boldsymbol{s} & \text{in } \Omega_e, \text{ and for } e = 1,\dots,\mathtt{n_{el}}, \\ \mathbf{E}\boldsymbol{\nabla}_{\mathtt{s}}\boldsymbol{u} = 0 & \text{in } \Omega_e, \text{ and for } e = 1,\dots,\mathtt{n_{el}}, \\ \boldsymbol{u} = \boldsymbol{u}_D & \text{on } \Gamma_D, \\ \mathbf{N}^T(\mathbf{D}^{1/2}\boldsymbol{L} + \mathbf{E}p) + (\boldsymbol{u}\otimes\boldsymbol{a})\boldsymbol{n} = -\boldsymbol{t} & \text{on } \Gamma_N, \\ [\![\boldsymbol{u}\otimes\boldsymbol{n}]\!] = \mathbf{0} & \text{on } \Gamma, \\ [\![\ \mathbf{N}^T(\mathbf{D}^{1/2}\boldsymbol{L} + \mathbf{E}p) + (\boldsymbol{u}\otimes\boldsymbol{a})\boldsymbol{n}]\!] = \mathbf{0} & \text{on } \Gamma, \end{cases} \tag{3.2.2}$$

By adding the convection term to the local and global problem of the Stokes equations, we have the local problems defined as

$$\begin{cases} \boldsymbol{L}_e + \mathbf{D}^{1/2}\boldsymbol{\nabla}_{\mathtt{s}}\boldsymbol{u}_e = \mathbf{0} & \text{in } \Omega_e \\ \boldsymbol{\nabla}_{\mathtt{s}}^T\mathbf{D}^{1/2}\boldsymbol{L}_e + \boldsymbol{\nabla}_{\mathtt{s}}^T\mathbf{E}\,p_e + \boldsymbol{\nabla}\cdot(\boldsymbol{u}_e\otimes\boldsymbol{a}) = \boldsymbol{s} & \text{in } \Omega_e \\ \mathbf{E}^T\boldsymbol{\nabla}_{\mathtt{s}}\boldsymbol{u}_e = 0 & \text{in } \Omega_e \\ \boldsymbol{u}_e = \boldsymbol{u}_D & \text{on } \partial\Omega_e \cap \Gamma_D, \\ \boldsymbol{u}_e = \hat{\boldsymbol{u}} & \text{on } \partial\Omega_e \setminus \Gamma_D, \end{cases} \tag{3.2.3}$$

Similar to the Stokes problem, an additional constraint is added to remove the indeterminacy of the pressure, namely

$$\frac{1}{|\partial\Omega_e|}\int_{\partial\Omega_e} \mathrm{p}_e d\Gamma = \rho_e$$

The trace of the velocity $\hat{\boldsymbol{u}}$ and the mean pressure $\boldsymbol{\rho}$ on the element boundaries are determined by solving the global problem accounting for the following transmission conditions and the Neumann boundary conditions

$$\begin{cases} [\![\mathbf{N}^T(\mathbf{D}^{1/2}\boldsymbol{L} + \mathbf{E}\,p) + (\boldsymbol{u}\otimes\boldsymbol{a})\boldsymbol{n}]\!] = \mathbf{0} & \text{on } \Gamma, \\ \mathbf{N}^T(\mathbf{D}^{1/2}\boldsymbol{L} + \mathbf{E}\,p) + (\boldsymbol{u}\otimes\boldsymbol{a})\boldsymbol{n} = -\boldsymbol{t} & \text{on } \Gamma_N, \end{cases} \tag{3.2.4}$$

The compatibility condition is utilized to close the global problem

$$\int_{\partial\Omega_e\setminus\Gamma_D} \mathbf{E}^T\mathbf{N}_e\hat{\boldsymbol{u}}d\Gamma + \int_{\partial\Omega_e\cap\Gamma_D} \mathbf{E}^T\mathbf{N}_e\boldsymbol{u}_D d\Gamma = 0$$

3.2.2 FCFV integral forms

For each cell $e = 1, \ldots, \mathtt{n_{el}}$, we calculate the integral form of the problem by applying the divergence theorem. The local problems reads as

$$\begin{aligned} &\int_{\Omega_e} \boldsymbol{L}_e^h d\Omega + \int_{\partial\Omega_e} \mathbf{N}_e^T\mathbf{D}^{1/2}\boldsymbol{u}_e^h d\Gamma = \mathbf{0} \\ &\int_{\partial\Omega_e} \mathbf{N}_e^T\widehat{(\mathbf{D}^{1/2}\boldsymbol{L}_e^h + \mathbf{E}p_e^h)}d\Gamma + \int_{\partial\Omega_e} \widehat{(\boldsymbol{u}_e^h\otimes\boldsymbol{a})}\boldsymbol{n}_e d\Gamma = \int_{\Omega_e} \boldsymbol{s}d\Omega \\ &\frac{1}{|\partial\Omega_e|}\int_{\partial\Omega_e} \mathrm{p}_e^h d\Gamma = \rho_e^h \end{aligned} \tag{3.2.5}$$

The diffusive numerical traces is defined as in Equation (2.3.11)

The trace of the convective flux can be defined as

$$\widehat{(\boldsymbol{u}_e^h\otimes\boldsymbol{a})}\boldsymbol{n}_e := \begin{cases} (\boldsymbol{u}_D\otimes\boldsymbol{a})\boldsymbol{n}_e + \tau^a(\boldsymbol{u}_e^h - \boldsymbol{u}_D) & \text{on } \partial\Omega_e\cap\Gamma_D, \\ (\hat{\boldsymbol{u}}^h\otimes\boldsymbol{a})\boldsymbol{n}_e + \tau^a(\boldsymbol{u}_e^h - \hat{\boldsymbol{u}}^h) & \text{elsewhere,} \end{cases} \tag{3.2.6}$$

where τ^a is the local stabilisation parameter related to the advection.

In order to describe the contribution of both the diffusion and convection terms to the stabilisation parameter, the diffusive part of the numerical fluxes is stabilized using a parameter proportional to the viscosity, whereas for the convection term the characteristic velocity field of the fluid is considered, namely

$$\tau^d = \kappa\frac{\nu}{\ell}, \quad \tau^a = \beta\|\boldsymbol{a}\|_{\mathcal{L}_2(\Omega)}$$

The definition of τ^d and κ have been already presented in Chapter2, whereas β is the scaling factor of τ^a. For the simplicity of notation in the following integral and matrix form, we define the total stabilisation parameter $\tau = \tau^a + \tau^d$ [40]. This choice is based on dimensional analysis which requires that τ has the same dimension unit as the velocity and

the ratio $\frac{\nu}{\ell}$ [36]. In this way, the stabilisation parameter takes into account the influence of both convection and diffusion phenomena of the problem. There are also other definitions of τ^a such as $\tau^a = \beta\|\boldsymbol{a}\|_2$ or the upwind type $\tau^a = \beta max\{0, \boldsymbol{a}\cdot\boldsymbol{n}\}$. The influence of these choices will be analysed afterwards.

After applying the trace of numerical flux and convection and the Dirichlet boundary conditions, the integral formulation of the local problems is as follows

$$\begin{aligned}
&\int_{\Omega_e} \boldsymbol{L}_e^h d\Omega + \int_{\partial\Omega_e\cap\Gamma_D} \mathbf{N}_e^T\mathbf{D}^{1/2}\boldsymbol{u}_D d\Gamma + \int_{\partial\Omega_e\setminus\Gamma_D} \mathbf{N}_e^T\mathbf{D}^{1/2}\hat{\boldsymbol{u}}^h d\Gamma = \mathbf{0}\\
&\int_{\partial\Omega_e} \mathbf{N}_e^T(\mathbf{D}^{1/2}\boldsymbol{L}_e^h + \mathbf{E}p_e^h)d\Gamma + \int_{\partial\Omega_e\cap\Gamma_D}(\boldsymbol{a}\cdot\boldsymbol{n}_e)\boldsymbol{u}_D d\Gamma + \int_{\partial\Omega_e\setminus\Gamma_D}(\boldsymbol{a}\cdot\boldsymbol{n}_e)\hat{\boldsymbol{u}}^h d\Gamma + \int_{\partial\Omega_e}\tau\boldsymbol{u}_e^h d\Gamma\\
&= \int_{\Omega_e}\boldsymbol{s}d\Omega + \int_{\partial\Omega_e\cap\Gamma_D}\tau\boldsymbol{u}_D d\Gamma + \int_{\partial\Omega_e\setminus\Gamma_D}\tau\hat{\boldsymbol{u}}^h d\Gamma\\
&\frac{1}{|\partial\Omega_e|}\int_{\partial\Omega_e} \mathrm{p}_e^h d\Gamma = \rho_e^h
\end{aligned} \tag{3.2.7}$$

Apply the divergence theorem in the momentum equation in Equation (3.2.7) again, it gives

$$\begin{aligned}
&\int_{\Omega_e} \boldsymbol{L}_e^h d\Omega + \int_{\partial\Omega_e\cap\Gamma_D} \mathbf{N}_e^T\mathbf{D}^{1/2}\boldsymbol{u}_D d\Gamma + \int_{\partial\Omega_e\setminus\Gamma_D} \mathbf{N}_e^T\mathbf{D}^{1/2}\hat{\boldsymbol{u}}^h d\Gamma = \mathbf{0}\\
&\int_{\Omega_e} (\boldsymbol{\nabla}_{\mathbf{s}}^T\mathbf{D}^{1/2}\boldsymbol{L}_e^h + \boldsymbol{\nabla}_{\mathbf{s}}^T\mathbf{E}p_e^h)d\Omega + \int_{\partial\Omega_e\cap\Gamma_D}(\boldsymbol{a}\cdot\boldsymbol{n}_e)\boldsymbol{u}_D d\Gamma + \int_{\partial\Omega_e\setminus\Gamma_D}(\boldsymbol{a}\cdot\boldsymbol{n}_e)\hat{\boldsymbol{u}}^h d\Gamma + \int_{\partial\Omega_e}\tau\boldsymbol{u}_e^h d\Gamma\\
&= \int_{\Omega_e}\boldsymbol{s}d\Omega + \int_{\partial\Omega_e\cap\Gamma_D}\tau\boldsymbol{u}_D d\Gamma + \int_{\partial\Omega_e\setminus\Gamma_D}\tau\hat{\boldsymbol{u}}^h d\Gamma\\
&\frac{1}{|\partial\Omega_e|}\int_{\partial\Omega_e} \mathrm{p}_e^h d\Gamma = \rho_e^h
\end{aligned} \tag{3.2.8}$$

Similarly, the integral form of the global problem reads as

$$\begin{aligned}
\sum_{e=1}^{\mathtt{nel}}\Big\{&\int_{\partial\Omega_e\cap\Gamma}(\mathbf{N}_e^T\widehat{(\mathbf{D}^{1/2}\boldsymbol{L}_e^h + \mathbf{E}p_e^h)} + \widehat{(\boldsymbol{u}_e^h\otimes\boldsymbol{a})}\boldsymbol{n}_e)d\Gamma\\
&+\int_{\partial\Omega_e\cap\Gamma_N}(\mathbf{N}_e^T\widehat{(\mathbf{D}^{1/2}\boldsymbol{L}_e^h + \mathbf{E}p_e^h)} + \widehat{(\boldsymbol{u}_e^h\otimes\boldsymbol{a})}\boldsymbol{n}_e + \boldsymbol{t})d\Gamma\Big\} = \mathbf{0}
\end{aligned} \tag{3.2.9}$$

Plug the equations of diffusive numerical traces and the flux of convection into Equation (3.2.10), the integral global form reads as

$$\begin{aligned}
\sum_{e=1}^{\mathtt{nel}}\Big\{&\int_{\partial\Omega_e\setminus\Gamma_D}(\mathbf{N}_e^T\mathbf{D}^{1/2}\boldsymbol{L}_e^h + \mathbf{N}_e^T\mathbf{E}p_e^h + (\hat{\boldsymbol{u}}^h\otimes\boldsymbol{a})\boldsymbol{n}_e)d\Gamma + \int_{\partial\Omega_e\setminus\Gamma_D}\tau\boldsymbol{u}_e^h d\Gamma - \int_{\partial\Omega_e\setminus\Gamma_D}\tau\hat{\boldsymbol{u}}^h d\Gamma\Big\}\\
&= -\sum_{e=1}^{\mathtt{nel}}\int_{\partial\Omega_e\cap\Gamma_N}\boldsymbol{t}d\Gamma
\end{aligned} \tag{3.2.10}$$

Equation (3.2.10) can be simplified with the following equation

$$\sum_{e=1}^{\mathtt{n_{el}}} \int_{\partial\Omega_e \setminus \Gamma_D} (\hat{\boldsymbol{u}} \otimes \boldsymbol{a}) \boldsymbol{n}_e d\Gamma = \sum_{e=1}^{\mathtt{n_{el}}} \int_{\partial\Omega_e \cap \Gamma_N} (\hat{\boldsymbol{u}} \otimes \boldsymbol{a}) \boldsymbol{n}_e d\Gamma \tag{3.2.11}$$

as $\hat{\boldsymbol{u}}$ and $\boldsymbol{a}$ are unique on the internal skeleton of the domain. This gives

$$\begin{aligned} \sum_{e=1}^{\mathtt{n_{el}}} \Big\{ \int_{\partial\Omega_e \setminus \Gamma_D} (\mathbf{N}_e^T \mathbf{D}^{1/2} \boldsymbol{L}_e^h + \mathbf{N}_e^T \mathbf{E} p_e^h) d\Gamma + \int_{\partial\Omega_e \setminus \Gamma_D} \tau \boldsymbol{u}_e^h d\Gamma - \int_{\partial\Omega_e \setminus \partial\Omega} \tau \hat{\boldsymbol{u}}^h d\Gamma \\ - \int_{\partial\Omega_e \cap \Gamma_N} (\tau - \boldsymbol{a} \cdot \boldsymbol{n}_e) \hat{\boldsymbol{u}}^h d\Gamma \Big\} = - \sum_{e=1}^{\mathtt{n_{el}}} \int_{\partial\Omega_e \cap \Gamma_N} \boldsymbol{t} d\Gamma \end{aligned} \tag{3.2.12}$$

As discussed before, the compatibility condition is included in the global form to close the problem

$$\int_{\partial\Omega_e \setminus \Gamma_D} \mathbf{E}^T \mathbf{N}_e \hat{\boldsymbol{u}} d\Gamma + \int_{\Omega_e \cap \Gamma_D} \mathbf{E}^T \mathbf{N}_e \boldsymbol{u}_D d\Gamma = 0 \tag{3.2.13}$$

3.2.3 FCFV linear system

For the sake of readability, henceforth the superscript h is omitted. With a degree of approximation $k = 0$ in each element for both $\boldsymbol{L}_e$,$\boldsymbol{u}_e$,p_e and also a degree of approximation $k = 0$ in each face/edge for $\hat{\boldsymbol{u}}$, the integral form of the local problem leads to

$$\begin{cases} -|\Omega_e| \mathbf{L}_e = \sum\limits_{j \in \mathcal{D}_e} |\boldsymbol{\Gamma}_{e,j}| \mathbf{D}^{1/2} \mathbf{N}_{e,j} \boldsymbol{u}_{D,j} + \sum\limits_{j \in \mathcal{B}_e} |\boldsymbol{\Gamma}_{e,j}| \mathbf{D}^{1/2} \mathbf{N}_{e,j} \hat{\mathbf{u}}_j \\ \sum\limits_{j \in \mathcal{A}_e} |\boldsymbol{\Gamma}_{e,j}| \tau_j \mathbf{u}_e = |\Omega_e| \boldsymbol{s}_e + \sum\limits_{j \in \mathcal{D}_e} |\boldsymbol{\Gamma}_{e,j}| (\tau_j - \boldsymbol{a} \cdot \boldsymbol{n}_j) \boldsymbol{u}_{D,j} + \sum\limits_{j \in \mathcal{B}_e} |\boldsymbol{\Gamma}_{e,j}| (\tau_j - \boldsymbol{a} \cdot \boldsymbol{n}_j) \hat{\mathbf{u}}_j \\ \mathrm{p}_e = \rho_e \end{cases} \tag{3.2.14}$$

In this way, $\boldsymbol{L}_e$ and $\boldsymbol{u}_e$ is decoupled and can be written as a function of $\hat{\boldsymbol{u}}$

$$\mathbf{L}_e = -|\Omega_e|^{-1} \boldsymbol{z}_e - |\Omega_e|^{-1} \sum_{j \in \mathcal{B}_e} |\boldsymbol{\Gamma}_{e,j}| \mathbf{D}^{1/2} \mathbf{N}_{e,j} \hat{\mathbf{u}}_j \tag{3.2.15a}$$

$$\mathbf{u}_e = \alpha_e^{-1} \boldsymbol{\beta}_e + \alpha_e^{-1} \sum_{j \in \mathcal{B}_e} |\boldsymbol{\Gamma}_{e,j}| (\tau_j - \boldsymbol{a}_j \cdot \boldsymbol{n}_j) \hat{\boldsymbol{u}}_j \tag{3.2.15b}$$

$$\mathrm{p}_e = \rho_e \tag{3.2.15c}$$

where

$$\alpha_e := \sum_{j \in \mathcal{A}_e} |\boldsymbol{\Gamma}_{e,j}| \tau_j \tag{3.2.16a}$$

$$\boldsymbol{\beta}_e := |\Omega_e| \boldsymbol{s}_e + \sum_{j \in \mathcal{D}_e} |\boldsymbol{\Gamma}_{e,j}| (\tau_j - \boldsymbol{a}_j \cdot \boldsymbol{n}_j) \boldsymbol{u}_{D,j} \tag{3.2.16b}$$

$$\boldsymbol{z}_e := \sum_{j \in \mathcal{D}_e} |\boldsymbol{\Gamma}_{e,j}| \mathbf{D}^{1/2} \mathbf{N}_{e,j} \boldsymbol{u}_{D,j} \tag{3.2.16c}$$

Similarly, the global problem can be written in terms of the global unknowns $\hat{\boldsymbol{u}}$ and ρ

$$\sum_{e=1}^{\mathtt{n_{el}}}\Big\{|\boldsymbol{\Gamma}_{e,i}|\mathbf{N}_{e,i}^T\mathbf{D}^{1/2}\mathbf{L}_e+|\boldsymbol{\Gamma}_{e,i}|\mathbf{E}^T\mathbf{N}_{e,i}\,\mathrm{p}_e+|\boldsymbol{\Gamma}_{e,i}|\tau_i\,\mathbf{u}_e-|\boldsymbol{\Gamma}_{e,i}|\tau_i\mathcal{X}_{\mathcal{I}e}(i)\,\hat{\mathbf{u}}_i-(\tau_i-\boldsymbol{a}_i\cdot\boldsymbol{n}_i)\mathcal{X}_{\mathcal{N}e}(i)\hat{\mathbf{u}}_i\Big\}$$
$$=-\sum_{e=1}^{\mathtt{n_{el}}}|\boldsymbol{\Gamma}_{e,i}|\boldsymbol{t}_i\mathcal{X}_{\mathcal{N}e}(i)\quad\text{for } i\in\mathcal{B}_e, \tag{3.2.17a}$$

$$\sum_{j\in\mathcal{B}_e}|\boldsymbol{\Gamma}_{e,j}|\mathbf{E}^T\mathbf{N}_{e,j}\hat{\mathbf{u}}=-\sum_{j\in\mathcal{D}_e}|\boldsymbol{\Gamma}_{e,j}|\mathbf{E}^T\mathbf{N}_{e,j}\boldsymbol{u}_{D,j}\quad\text{for } e=1,\ldots,\mathtt{n_{el}}\ , \tag{3.2.17b}$$

By plugging Equation (3.2.15) into Equation (3.2.17), the global problem can be written in terms of the global unknowns $\hat{\boldsymbol{u}}$ and ρ. The following linear system is obtained:

$$\begin{bmatrix}\hat{\mathbf{K}}_{\hat{u}\hat{u}}+\hat{\mathbf{C}}_{\hat{u}\hat{u}} & \hat{\mathbf{K}}_{\hat{u}\rho}\\ \hat{\mathbf{K}}_{\hat{u}\rho}^T & \mathbf{0}_{\mathtt{n_{el}}}\end{bmatrix}\begin{Bmatrix}\hat{\mathbf{u}}\\ \boldsymbol{\rho}\end{Bmatrix}=\begin{Bmatrix}\hat{\mathbf{f}}_{\hat{u}}\\ \hat{\mathbf{f}}_{\rho}\end{Bmatrix} \tag{3.2.18}$$

where

$$\begin{aligned}
(\hat{\mathbf{K}}_{\hat{u}\hat{u}})_{i,j}^e &:= |\boldsymbol{\Gamma}_{e,i}|(|\boldsymbol{\Gamma}_{e,j}|\alpha_e^{-1}\tau_i\tau_j\boldsymbol{I}_{\mathtt{n_{sd}}}-|\boldsymbol{\Gamma}_{e,j}||\Omega_e|^{-1}\mathbf{N}_{e,i}^T\mathbf{D}^{1/2}\mathbf{D}^{1/2}\mathbf{N}_{e,j}-\tau_i\delta_{ij}\boldsymbol{I}_{\mathtt{n_{sd}}})\\
(\hat{\mathbf{C}}_{\hat{u}\hat{u}})_{i,j}^e &:= |\boldsymbol{\Gamma}_{e,i}|(-|\boldsymbol{\Gamma}_{e,j}|\alpha_e^{-1}\tau_i\boldsymbol{a}_j\cdot\boldsymbol{n}_j+\boldsymbol{a}_i\cdot\boldsymbol{n}_i\mathcal{X}_{\mathcal{N}e}(i)\delta_{ij})\boldsymbol{I}_{\mathtt{n_{sd}}}\\
(\hat{\mathbf{K}}_{\hat{u}\rho})_i^e &:= |\boldsymbol{\Gamma}_{e,i}|\mathbf{E}^T\mathbf{N}_{e,i}\\
(\hat{\mathbf{f}}_{\hat{u}})_i^e &:= -|\boldsymbol{\Gamma}_{e,i}|\boldsymbol{t}\mathcal{X}_{\mathcal{N}e}(i)+|\Omega_e|^{-1}|\boldsymbol{\Gamma}_{e,i}|\mathbf{N}_{e,i}^T\mathbf{D}^{1/2}\boldsymbol{z}_e-|\boldsymbol{\Gamma}_{e,i}|\tau_i\,\alpha_e^{-1}\boldsymbol{\beta}_e\\
(\hat{\mathbf{f}}_{\rho})^e &:= -\sum_{i\in\mathcal{D}_e}|\boldsymbol{\Gamma}_{e,j}|\mathbf{E}^T\mathbf{N}_{e,j}\boldsymbol{u}_{D,j}
\end{aligned} \tag{3.2.19}$$

for $i,j\in\mathcal{B}_e$. Compared with the matrix form we obtained for the Stokes problem, one can observe that the only difference is the introduction of the convection matrix $\hat{\mathbf{C}}$ and the modification of the vector β_e on the right-hand side.

3.3 Numerical studies

In this section, a rotating flow example is utilized to validate the FCFV method for the Oseen problem. Simulations are done on meshes of different sizes and the accuracy of the results are analysed. The convergence rate of $\mathcal{L}_2$ norm of the error are checked on both primal and mixed variables. At last, a detailed analysis is done about the influence of different choices of the stabilisation parameter on the accuracy of the results.

3.3.1 Optimal convergence rate of the primal and mixed variables

The analytical solution of the rotating flow example is

$$\begin{cases} u_1(\boldsymbol{x}) = (1 - \cos(2\pi x)) \sin(2\pi y) \\ u_2(\boldsymbol{x}) = -\sin(2\pi x)(1 - \cos(2\pi y)) \\ p(\boldsymbol{x}) = \cos(\pi x) + \cos(\pi y) \end{cases} \tag{3.3.1}$$

in the square domain $\Omega = [0, 1]^2$. The source term and boundary conditions are chosen to reproduce the above analytical solution and the convective field $\boldsymbol{a}$ is defined using the expression of $\boldsymbol{u}$ in (3.3.1). In this case, all Dirichlet boundary conditions are set. The plots of the analytical velocity and pressure fields are demonstrated in Figure 3.1.

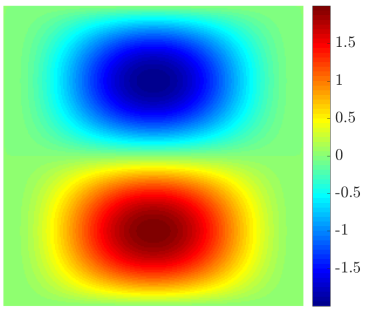

(a) u_1

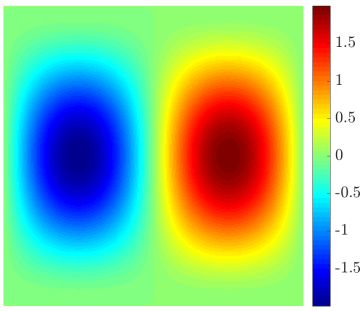

(b) u_2

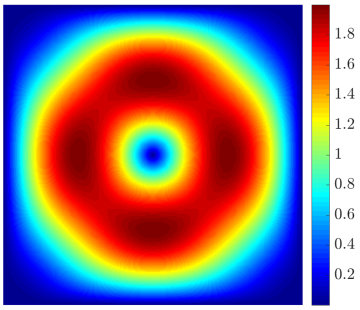

(c) $\|\boldsymbol{u}\|_2$

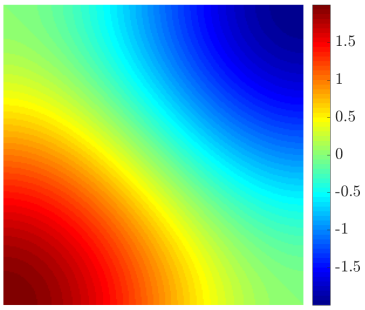

(d) p

Figure 3.1: Analytical solution of rotating flow

Figure 3.2 and 3.3 show the velocity and pressure fields from the numerical solution. The plots of eighth order meshes are in good agreement with the analytical ones. For the lower level mesh, it can be seen that the discrepancy of the numerical pressure fields from the analytical one is more obvious than that of the velocity fields. Similar phenomenon has also been observed in the Stokes problem. If we refine the mesh to the eighth level, the method can reproduce accurate pressure fields for both triangular and quadrilateral meshes.

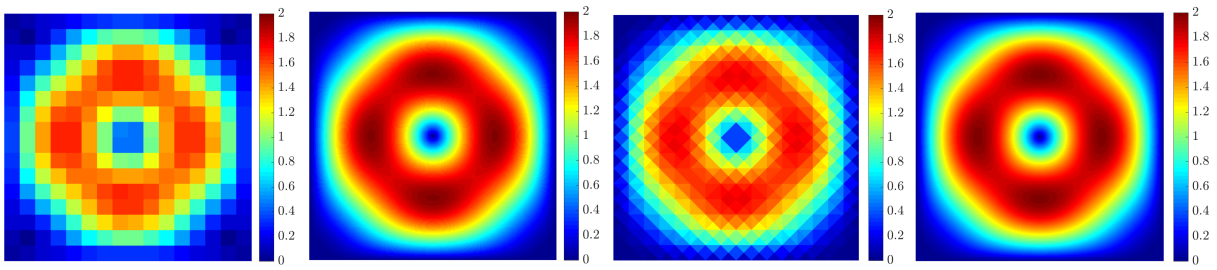

(a) QUA H4 (b) QUA H8 (c) TRI H4 (d) TRI H8

Figure 3.2: Numerical approximation of the module of velocity(QUA: quadrilateral mesh, TRI: triangular mesh; H4: fourth level refinement, H8: eighth level refinement)

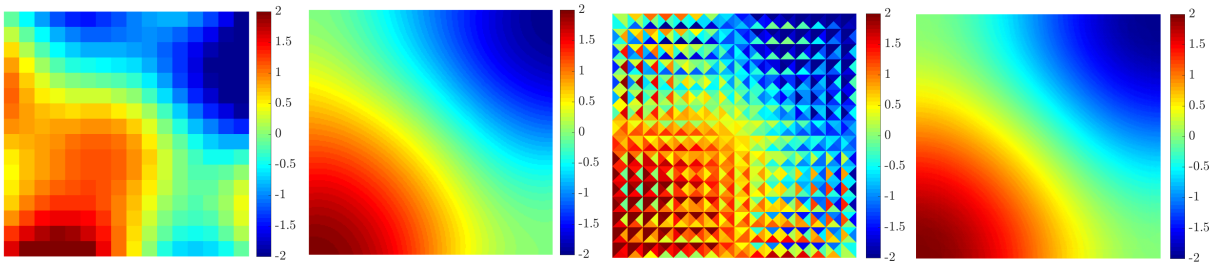

(a) QUA H4 (b) QUA H8 (c) TRI H4 (d) TRI H8

Figure 3.3: Numerical approximation of the pressure field (QUA: quadrilateral mesh, TRI: triangular mesh; H4: fourth level refinement, H8: eighth level refinement)

Figure 3.4 shows the convergence rate of the rotating flow example with $\tau^d = 10\frac{\nu}{\ell}$, $\tau^a = \|\boldsymbol{a}\|_{\mathcal{L}_2(\Omega)}$. Optimal first-order convergence rates of all the variables are achieved with both triangular and quadrilateral meshes.

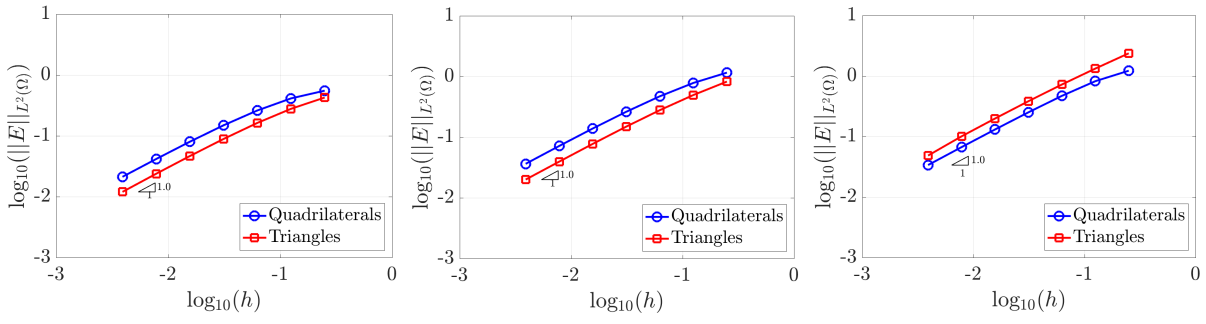

(a) $\boldsymbol{u}$ (b) $\boldsymbol{L}$ (c) p

Figure 3.4: Convergence rate of the rotating flow problem

3.3.2 Influence of the convection stabilisation parameter

The diffusive part of the numerical fluxes has already been studied in the Stokes problem. In this section, we consider only the influence of the convection stabilisation parameter by choosing $\kappa = 10$ for τ^d, and analyse the influence of β on the accuracy of the results, which is represented with the $\mathcal{L}_2$ norm of the error. Figure 3.5,3.6,3.7 illustrate the sensitivity studies on the above examples using different definition of τ^a. It can be observed that the method is robust with respect to the choice of stabilisation parameters. In the range 0.1-1, relatively accurate velocity, pressure and strain tensor can be obtained for all type of definitions of τ^a.

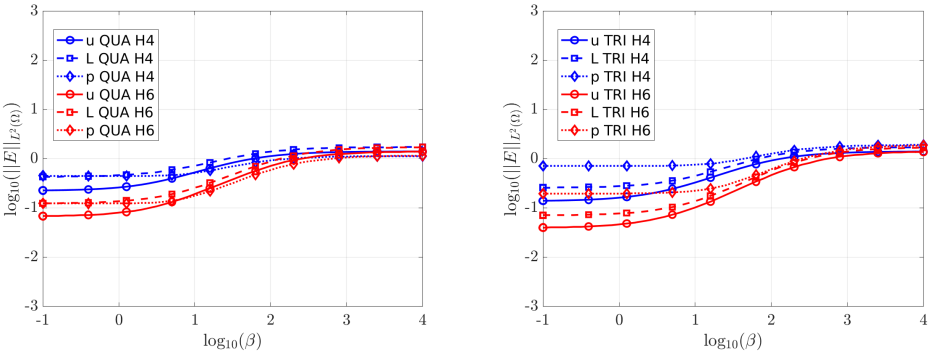

(a) Quadrilateral mesh (b) Ex1 Triangular mesh

Figure 3.5: Error evolution of $\boldsymbol{u}$, p and $\boldsymbol{L}$ as a function of $\tau^a = \beta\|\boldsymbol{a}\|_{\mathcal{L}_2(\Omega)}$

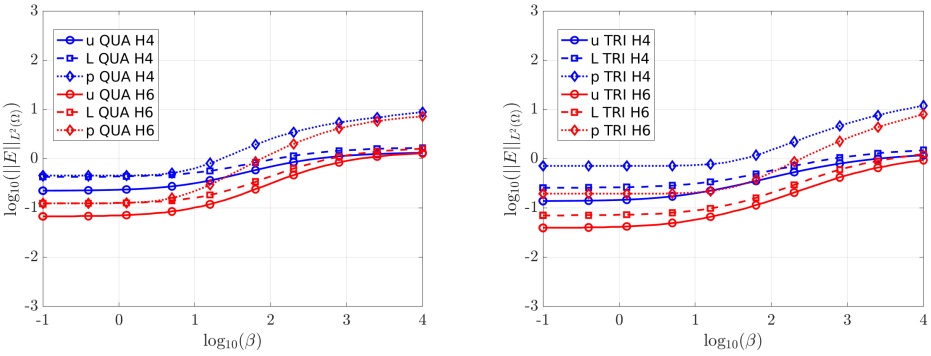

(a) Ex1 Quadrilateral mesh (b) Ex1 Triangular mesh

Figure 3.6: Error evolution of $\boldsymbol{u}$, p and $\boldsymbol{L}$ as a function with $\tau^a = \beta \max\{\boldsymbol{a} \cdot \boldsymbol{n}, 0\}$

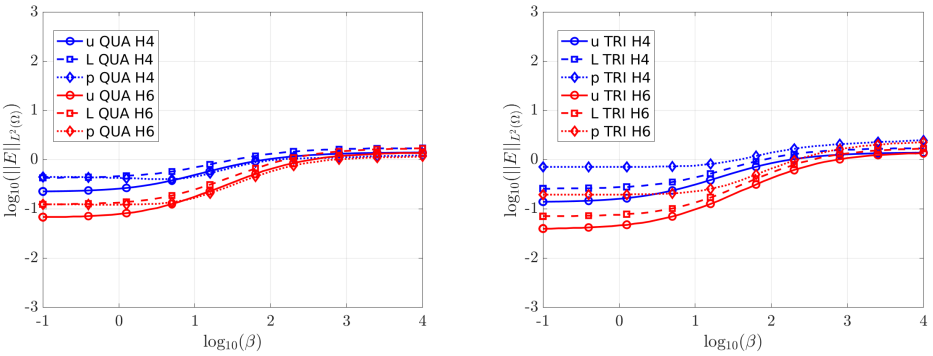

(a) Ex1 Quadrilateral mesh

(b) Ex1 Triangular mesh

Figure 3.7: Error evolution of $\boldsymbol{u}$, p and $\boldsymbol{L}$ as a function of $\tau^a = \|\boldsymbol{a}\|_2$

Chapter 4

FCFV method for the steady incompressible Navier-Stokes equations

In this chapter, the steady-state incompressible Navier-Stokes equations are studied. The work done for Oseen problems is used as the stepping stone to the implementation of FCFV for Navier-Stokes problems. The derivation of integral and matrix form is similar, thus only attention is focused on the nonlinear convective term. The Newton-Raphson method is used to solve the nonlinear global system. Two examples are analysed to validate the method – one is a 2D example with analytical solution and the other one is the well-known benchmark test of the lid-driven cavity flow.

4.1 Governing equations of the Navier-Stokes flow

Consider a Navier-Stokes problem with Dirichlet and Neumann boundary conditions. The strong form of the boundary value problem can be written as

$$\begin{cases} -\boldsymbol{\nabla}\cdot(2\nu\boldsymbol{\nabla}^{\mathrm{s}}\boldsymbol{u}-p\boldsymbol{I}_{\mathrm{n_{sd}}})+\boldsymbol{\nabla}\cdot(\boldsymbol{u}\otimes\boldsymbol{u})=\boldsymbol{s} & \text{in } \Omega,\\ \boldsymbol{\nabla}\cdot\boldsymbol{u}=0 & \text{in } \Omega,\\ \boldsymbol{u}=\boldsymbol{u}_D & \text{on } \Gamma_D,\\ \boldsymbol{n}\cdot\big(2\nu\boldsymbol{\nabla}^{\mathrm{s}}\boldsymbol{u}-p\boldsymbol{I}_{\mathrm{n_{sd}}}\big)-(\boldsymbol{u}\otimes\boldsymbol{u})\boldsymbol{n}=\boldsymbol{t} & \text{on } \Gamma_N, \end{cases} \tag{4.1.1}$$

Compared with the strong form of the Oseen problem, the only difference is that $\boldsymbol{a}$ is changed to $\boldsymbol{u}$, which gives a nonlinear convection term.

4.2 The FCFV framework

The derivation of the FCFV formulations of the Navier-Stokes equations is similar to what we have done in the Oseen problems. The only difference is the advection term, which is nonlinear in the Navier-Stokes problems. This will generate a nonlinear global system to be solved using the Newton-Raphson algorithm.

4.2.1 FCFV strong forms

We can rewrite Equation (4.1.1) into the Voigt form

$$\begin{cases} -\boldsymbol{\nabla}_{\mathbf{s}}^T(\mathbf{D}\boldsymbol{\nabla}_{\mathbf{s}}\boldsymbol{u} - \mathbf{E}p) + \boldsymbol{\nabla}\cdot(\boldsymbol{u}\otimes\boldsymbol{u}) = \boldsymbol{s} & \text{in } \Omega, \\ \mathbf{E}^T\boldsymbol{\nabla}_{\mathbf{s}}\boldsymbol{u} = 0 & \text{in } \Omega, \\ \boldsymbol{u} = \boldsymbol{u}_D & \text{on } \Gamma_D, \\ \mathbf{N}^T(\mathbf{D}\boldsymbol{\nabla}_{\mathbf{s}}\boldsymbol{u} - \mathbf{E}p) - (\boldsymbol{u}\otimes\boldsymbol{u})\boldsymbol{n} = \boldsymbol{t} & \text{on } \Gamma_N, \end{cases} \tag{4.2.1}$$

The local and global problems of the Navier-Stokes equations can be easily obtained by replacing the linear convection term in the Oseen problem with the nonlinear one.

The local problem of the Navier-Stokes equations becomes

$$\begin{cases} \boldsymbol{L}_e + \mathbf{D}^{1/2}\boldsymbol{\nabla}_{\mathbf{s}}\boldsymbol{u}_e = \mathbf{0} & \text{in } \Omega_e \\ \boldsymbol{\nabla}_{\mathbf{s}}^T\mathbf{D}^{1/2}\boldsymbol{L}_e + \boldsymbol{\nabla}_{\mathbf{s}}^T\mathbf{E}\,p_e + \boldsymbol{\nabla}\cdot(\boldsymbol{u}_e\otimes\boldsymbol{u}_e) = \boldsymbol{s} & \text{in } \Omega_e \\ \mathbf{E}^T\boldsymbol{\nabla}_{\mathbf{s}}\boldsymbol{u}_e = 0 & \text{in } \Omega_e \\ \boldsymbol{u}_e = \boldsymbol{u}_D & \text{on } \partial\Omega_e\cap\Gamma_D, \\ \boldsymbol{u}_e = \hat{\boldsymbol{u}} & \text{on } \partial\Omega_e\setminus\Gamma_D, \end{cases} \tag{4.2.2}$$

As explained in Oseen problems, an additional constraint has be added to remove the indeterminacy of the pressure in the local problem, namely

$$\frac{1}{|\partial\Omega_e|}\int_{\partial\Omega_e}\mathrm{p}_e d\Gamma = \rho_e$$

The global problem reads as

$$\begin{cases} [\![\mathbf{N}^T(\mathbf{D}^{1/2}\boldsymbol{L} + \mathbf{E}\,p) + (\boldsymbol{u}\otimes\boldsymbol{u})\boldsymbol{n}]\!] = \mathbf{0} & \text{on } \Gamma, \\ \mathbf{N}^T(\mathbf{D}^{1/2}\boldsymbol{L} + \mathbf{E}\,p) + (\boldsymbol{u}\otimes\boldsymbol{u})\boldsymbol{n} = -\boldsymbol{t} & \text{on } \Gamma_N, \end{cases} \tag{4.2.3}$$

The same compatibility condition is included here to close the global problem.

$$\int_{\partial\Omega_e\setminus\Gamma_D}\mathbf{E}^T\mathbf{N}_e\hat{\boldsymbol{u}}d\Gamma + \int_{\partial\Omega_e\cap\Gamma_D}\mathbf{E}^T\mathbf{N}_e\boldsymbol{u}_D d\Gamma = 0$$

4.2.2 FCFV integral forms

For each cell $e = 1, \ldots, \mathtt{n_{el}}$, we calculate the integral form of the problem by applying the divergence theorem. The local problems read as

$$\begin{aligned}
&\int_{\partial\Omega_e} \boldsymbol{L}_e^h d\Gamma + \int_{\partial\Omega_e} \mathbf{N}_e^T \mathbf{D}^{1/2} \boldsymbol{u}_e^h d\Gamma = \mathbf{0} \\
&\int_{\Omega_e} \mathbf{N}_e^T (\widehat{\mathbf{D}^{1/2}\boldsymbol{L}_e^h + \mathbf{E}p_e^h}) d\Omega + \int_{\partial\Omega_e} (\widehat{\boldsymbol{u}_e^h \otimes \boldsymbol{u}_e^h}) \boldsymbol{n}_e d\Gamma = \int_{\Omega_e} \boldsymbol{s} d\Omega \\
&\frac{1}{|\partial\Omega_e|} \int_{\partial\Omega_e} \mathrm{p}_e^h d\Gamma = \rho_e^h
\end{aligned} \tag{4.2.4}$$

For convection, several alternatives are possible, and they can be written in general form as

$$(\widehat{\boldsymbol{u}_e \otimes \boldsymbol{u}_e})\boldsymbol{n}_e := \begin{cases} (\boldsymbol{u}_D \otimes \boldsymbol{u}_D)\boldsymbol{n}_e + \tau^a(\boldsymbol{u}_e - \boldsymbol{u}_D) & \text{on } \partial\Omega_e \cap \Gamma_D, \\ (\hat{\boldsymbol{u}} \otimes \hat{\boldsymbol{u}})\boldsymbol{n}_e + \tau^a(\boldsymbol{u}_e - \hat{\boldsymbol{u}}) & \text{elsewhere,} \end{cases} \tag{4.2.5}$$

where $\tau^a = \beta \|\boldsymbol{u}\|_{\mathcal{L}_2(\Omega)}$. Other definitions of τ^a is also applicable such as $\tau^a = \beta \|\hat{\boldsymbol{u}}\|_2$ or the upwind type $\tau^a = \beta max\{0, \hat{\boldsymbol{u}} \cdot \boldsymbol{n}\}$. The stabilization utilized in the integral form of the local and global problems, is $\tau = \tau^d + \tau^a$.

The local problem of the Navier-Stokes equations differs from the Oseen equations only in the momentum equation, where $\boldsymbol{a}$ is substituted with $\boldsymbol{u}_D$ on the Dirichlet boundary and $\hat{\boldsymbol{u}}$ on the internal skeleton and non-Dirichlet boundary.

$$\begin{aligned}
&\int_{\Omega_e} \boldsymbol{L}_e^h d\Omega + \int_{\partial\Omega_e \cap \Gamma_D} \mathbf{N}_e^T \mathbf{D}^{1/2} \boldsymbol{u}_D d\Gamma + \int_{\partial\Omega_e \setminus \Gamma_D} \mathbf{N}_e^T \mathbf{D}^{1/2} \hat{\boldsymbol{u}}^h d\Gamma = \mathbf{0} \\
&\int_{\partial\Omega_e} \mathbf{N}_e^T (\mathbf{D}^{1/2}\boldsymbol{L}_e^h + \mathbf{E}p_e^h) d\Gamma + \int_{\partial\Omega_e \cap \Gamma_D} (\boldsymbol{u}_D \cdot \boldsymbol{n}_e)\boldsymbol{u}_D d\Gamma + \int_{\partial\Omega_e \setminus \Gamma_D} (\hat{\boldsymbol{u}}^h \cdot \boldsymbol{n}_e)\hat{\boldsymbol{u}}^h d\Gamma + \int_{\partial\Omega_e} \tau \boldsymbol{u}_e^h d\Gamma \\
&= \int_{\Omega_e} \boldsymbol{s} d\Omega + \int_{\partial\Omega_e \cap \Gamma_D} \tau \boldsymbol{u}_D d\Gamma + \int_{\partial\Omega_e \setminus \Gamma_D} \tau \hat{\boldsymbol{u}}^h d\Gamma \\
&\frac{1}{|\partial\Omega_e|} \int_{\partial\Omega_e} p_e^h d\Gamma = \rho_e^h
\end{aligned} \tag{4.2.6}$$

Analogously, the global problem reads as

$$\begin{aligned}
\sum_{e=1}^{\mathtt{n_{el}}} \Big\{ &\int_{\partial\Omega_e \setminus \Gamma_D} (\mathbf{N}_e^T \mathbf{D}^{1/2} \boldsymbol{L}_e^h + \mathbf{N}_e^T \mathbf{E} p_e^h) d\Gamma + \int_{\partial\Omega_e \setminus \Gamma_D} \tau \boldsymbol{u}_e^h d\Gamma - \int_{\partial\Omega_e \setminus \partial\Omega} \tau \hat{\boldsymbol{u}}^h d\Gamma \\
&- \int_{\partial\Omega_e \cap \Gamma_N} (\tau - \hat{\boldsymbol{u}}^h \cdot \boldsymbol{n}_e)\hat{\boldsymbol{u}}^h d\Gamma \Big\} = -\sum_{e=1}^{\mathtt{n_{el}}} \int_{\partial\Omega_e \cap \Gamma_N} \boldsymbol{t} \Gamma
\end{aligned} \tag{4.2.7}$$

4.2.3 FCFV linear system

The closed form expression for $\boldsymbol{L}_e$ and $\boldsymbol{u}_e$ as a function of $\hat{\boldsymbol{u}}$ is obtained by substituting $\boldsymbol{a}$ with $\boldsymbol{u}_D$ on the Dirichlet boundary and $\hat{\boldsymbol{u}}$ on the internal skeleton and non-Dirichlet

boundary

$$\mathbf{L}_e = -|\Omega_e|^{-1}\boldsymbol{z}_e - |\Omega_e|^{-1}\sum_{j\in\mathcal{B}_e}|\boldsymbol{\Gamma}_{e,j}|\mathbf{D}^{1/2}\mathbf{N}_{e,j}\hat{\mathbf{u}}_j \tag{4.2.8a}$$

$$\mathbf{u}_e = \alpha_e^{-1}\boldsymbol{\beta}_e + \alpha_e^{-1}\sum_{j\in\mathcal{B}_e}|\boldsymbol{\Gamma}_{e,j}|(\tau_j - \hat{\mathbf{u}}_j\cdot\boldsymbol{n}_j)\hat{\mathbf{u}}_j \tag{4.2.8b}$$

$$\mathrm{p}_e = \rho_e \tag{4.2.8c}$$

where

$$\alpha_e := \sum_{j\in\mathcal{A}_e}|\boldsymbol{\Gamma}_{e,j}|\tau_j \tag{4.2.9a}$$

$$\boldsymbol{\beta}_e := |\Omega_e|\boldsymbol{s}_e + \sum_{j\in\mathcal{D}_e}|\boldsymbol{\Gamma}_{e,j}|(\tau_j - \boldsymbol{u}_{D,j}\cdot\boldsymbol{n}_j)\boldsymbol{u}_{D,j} \tag{4.2.9b}$$

$$\boldsymbol{z}_e := \sum_{j\in\mathcal{D}_e}|\boldsymbol{\Gamma}_{e,j}|\mathbf{D}^{1/2}\mathbf{N}_{e,j}\boldsymbol{u}_{D,j} \tag{4.2.9c}$$

Similarly, the global system reads as

$$\sum_{e=1}^{\mathtt{n_{el}}}\Big\{|\boldsymbol{\Gamma}_{e,i}|\mathbf{N}_{e,i}^T\mathbf{D}^{1/2}\mathbf{L}_e + |\boldsymbol{\Gamma}_{e,i}|\mathbf{E}^T\mathbf{N}_{e,i}\,\mathrm{p}_e + |\boldsymbol{\Gamma}_{e,i}|\tau_i\,\mathbf{u}_e - |\boldsymbol{\Gamma}_{e,i}|\tau_i\,\mathcal{X}_{\mathcal{I}e}(i)\hat{\boldsymbol{u}}_i - |\boldsymbol{\Gamma}_{e,i}|(\tau_i - \hat{\boldsymbol{u}}_i\cdot\boldsymbol{n})\,\mathcal{X}_{\mathcal{N}e}(i)\hat{\boldsymbol{u}}_i\Big\} = -\sum_{e=1}^{\mathtt{n_{el}}}|\boldsymbol{\Gamma}_{e,i}|\boldsymbol{t}\mathcal{X}_{\mathcal{N}e}(i) \quad \text{for } i\in\boldsymbol{\mathcal{B}}_e, \tag{4.2.10a}$$

$$\sum_{j\in\mathcal{B}_e}|\boldsymbol{\Gamma}_{e,j}|\mathbf{E}^T\mathbf{N}_{e,j}\hat{\mathbf{u}}_j = -\sum_{j\in\mathcal{D}_e}|\boldsymbol{\Gamma}_{e,j}|\mathbf{E}^T\mathbf{N}_{e,j}\boldsymbol{u}_{D,j} \;\text{ for } e = 1,\ldots,\mathtt{n_{el}}\;, \tag{4.2.10b}$$

By plugging Equation (4.2.8) into (4.2.10), the global problem will be a nonlinear linear system of equations of the unknowns $\hat{\boldsymbol{u}}$ and ρ.

$$\begin{bmatrix}\hat{\mathbf{K}}_{\hat{u}\hat{u}} + \hat{\mathbf{C}}_{\hat{u}\hat{u}}(\hat{\boldsymbol{u}}) & \hat{\mathbf{K}}_{\hat{u}\rho}\\ \hat{\mathbf{K}}_{\hat{u}\rho}^T & \mathbf{0}_{\mathtt{n_{el}}}\end{bmatrix}\begin{Bmatrix}\hat{\mathbf{u}}\\ \boldsymbol{\rho}\end{Bmatrix} = \begin{Bmatrix}\hat{\mathbf{f}}_{\hat{u}}\\ \hat{\mathbf{f}}_{\rho}\end{Bmatrix} \tag{4.2.11}$$

where

$$(\hat{\mathbf{K}}_{\hat{u}\hat{u}})_{i,j}^e := |\boldsymbol{\Gamma}_{e,i}|(|\boldsymbol{\Gamma}_{e,j}|\alpha_e^{-1}\tau_i\tau_j\boldsymbol{I}_{\mathtt{n_{sd}}} - |\boldsymbol{\Gamma}_{e,j}||\Omega_e|^{-1}\mathbf{N}_{e,i}^T\mathbf{D}^{1/2}\mathbf{D}^{1/2}\mathbf{N}_{e,j} - \tau_i\delta_{ij}\boldsymbol{I}_{\mathtt{n_{sd}}}) \tag{4.2.12a}$$

$$(\hat{\mathbf{C}}_{\hat{u}\hat{u}})_{i,j}^e := |\boldsymbol{\Gamma}_{e,i}|(-|\boldsymbol{\Gamma}_{e,j}|\alpha_e^{-1}\tau_i\hat{\mathbf{u}}_j\cdot\boldsymbol{n}_j + \hat{\mathbf{u}}_i\cdot\boldsymbol{n}_i\mathcal{X}_{\mathcal{N}e}(i)\delta_{ij})\boldsymbol{I}_{\mathtt{n_{sd}}} \tag{4.2.12b}$$

$$(\hat{\mathbf{K}}_{\hat{u}\rho})_i^e := |\boldsymbol{\Gamma}_{e,i}|\mathbf{E}^T\mathbf{N}_{e,i} \tag{4.2.12c}$$

$$(\hat{\mathbf{f}}_{\hat{u}})_i^e := -|\boldsymbol{\Gamma}_{e,i}|\boldsymbol{t}\mathcal{X}_{\mathcal{N}e}(i) + |\Omega_e|^{-1}|\boldsymbol{\Gamma}_{e,i}|\mathbf{N}_{e,i}^T\mathbf{D}^{1/2}\boldsymbol{z}_e - |\boldsymbol{\Gamma}_{e,i}|\tau_i\,\alpha_e^{-1}\boldsymbol{\beta}_e \tag{4.2.12d}$$

$$(\hat{\mathbf{f}}_{\rho})^e := -\sum_{j\in\mathcal{D}_e}|\boldsymbol{\Gamma}_{e,j}|\mathbf{E}^T\mathbf{N}_{e,j}\boldsymbol{u}_{D,j} \tag{4.2.12e}$$

for $i,j\in\mathcal{B}_e$.

4.3 Newton-Raphson procedure

The only non-linear part is the global matrix form. In the following section, we apply Newton-Raphson method to solve the global problem.
The residuals are defined as

$$\begin{aligned} \boldsymbol{r}_{\hat{u}} &:= \hat{\mathbf{K}}_{\hat{u}\hat{u}}\hat{\boldsymbol{u}} + \hat{\mathbf{C}}_{\hat{u}\hat{u}}(\hat{\boldsymbol{u}})\hat{\boldsymbol{u}} + \hat{\mathbf{K}}_{\hat{u}\rho}\boldsymbol{\rho} - \hat{\mathbf{f}}_{\hat{u}} \\ \boldsymbol{r}_{\rho} &:= \hat{\mathbf{K}}_{\hat{u}\rho}^{T}\hat{\boldsymbol{u}} - \hat{\mathbf{f}}_{\rho} \end{aligned} \tag{4.3.1}$$

The linearized problem obtained from the FCFV discretisation of Navier-Stokes equations is

$$\begin{bmatrix} \hat{\mathbf{K}}_{\hat{u}\hat{u}} + \hat{\mathbf{A}}^{r}_{\hat{u}\hat{u}} & \hat{\mathbf{K}}_{\hat{u}\rho} \\ \hat{\mathbf{K}}^{T}_{\hat{u}\rho} & \mathbf{0}_{\mathtt{n_{el}}} \end{bmatrix} \begin{Bmatrix} \triangle\hat{\mathbf{u}}^{r} \\ \triangle\boldsymbol{\rho}^{r} \end{Bmatrix} = - \begin{Bmatrix} \boldsymbol{r}^{r}_{\hat{u}} \\ \boldsymbol{r}_{\rho} \end{Bmatrix} \tag{4.3.2}$$

where

$$\hat{\mathbf{A}}^{r}_{\hat{u}\hat{u}} = \frac{d}{d\hat{\boldsymbol{u}}}[\hat{\mathbf{C}}_{\hat{u}\hat{u}}(\hat{\boldsymbol{u}})\hat{\boldsymbol{u}}]|_{\hat{\boldsymbol{u}}=\hat{\boldsymbol{u}}^{r}} \tag{4.3.3}$$

The previous equations may be rewritten as follows

$$\begin{aligned} \hat{\mathbf{K}}_{\hat{u}\hat{u}}(\hat{\boldsymbol{u}}^{r+1} - \cancel{\hat{\boldsymbol{u}}^{r}}) + \hat{\mathbf{A}}^{r}_{\hat{u}\hat{u}}(\hat{\boldsymbol{u}}^{r+1} - \hat{\boldsymbol{u}}^{r}) + \hat{\mathbf{K}}_{\hat{u}\rho}(\boldsymbol{\rho}^{r+1} - \cancel{\boldsymbol{\rho}^{r}}) = \\ - (\cancel{\hat{\mathbf{K}}_{\hat{u}\hat{u}}\hat{\boldsymbol{u}}^{r}} + \hat{\mathbf{C}}_{\hat{u}\hat{u}}(\hat{\boldsymbol{u}}^{r})\hat{\boldsymbol{u}}^{r} + \cancel{\hat{\mathbf{K}}_{\hat{u}\rho}\boldsymbol{\rho}^{r}} - \hat{\mathbf{f}}_{\hat{u}}) \\ \hat{\mathbf{K}}^{r}_{\hat{u}\rho}(\hat{\boldsymbol{u}}^{r+1} - \cancel{\hat{\boldsymbol{u}}^{r}}) = -(\cancel{\hat{\mathbf{K}}^{T}_{\hat{u}\rho}\hat{\boldsymbol{u}}^{r}} - \hat{\mathbf{f}}_{\rho}) \end{aligned} \tag{4.3.4}$$

Consequently, this simplified system is obtained

$$\begin{bmatrix} \hat{\mathbf{K}}_{\hat{u}\hat{u}} + \hat{\mathbf{A}}^{r}_{\hat{u}\hat{u}} & \hat{\mathbf{K}}_{\hat{u}\rho} \\ \hat{\mathbf{K}}^{T}_{\hat{u}\rho} & \mathbf{0}_{\mathtt{n_{el}}} \end{bmatrix} \begin{Bmatrix} \hat{\mathbf{u}}^{r+1} \\ \boldsymbol{\rho}^{r+1} \end{Bmatrix} = - \begin{Bmatrix} \hat{\boldsymbol{r}}^{r}_{\hat{u}} \\ \hat{\mathbf{f}}_{\rho} \end{Bmatrix} \tag{4.3.5}$$

where $\hat{\boldsymbol{r}}^{r}_{\hat{u}} := \hat{\mathbf{f}}_{\hat{u}} - \hat{\mathbf{C}}_{\hat{u}\hat{u}}(\hat{\boldsymbol{u}}^{r})\hat{\boldsymbol{u}}^{r} + \hat{\mathbf{A}}^{r}_{\hat{u}\hat{u}}\hat{\boldsymbol{u}}^{r}$.

Recall that $(\hat{\mathbf{C}}_{\hat{u}\hat{u}})^{e}_{i,j} := |\boldsymbol{\Gamma}_{e,i}|(-|\boldsymbol{\Gamma}_{e,j}|\alpha_{e}^{-1}\tau_{i}\hat{\mathbf{u}}_{j}\cdot\boldsymbol{n}_{j} + \hat{\mathbf{u}}_{i}\cdot\boldsymbol{n}_{i}\mathcal{X}_{\mathcal{N}e}(i)\delta_{ij})\boldsymbol{I}_{\mathtt{n_{sd}}}$.
Thus, we have

$$(\hat{\mathbf{C}}_{\hat{u}\hat{u}})^{e}_{i,j}\hat{\boldsymbol{u}}_{j} = -|\boldsymbol{\Gamma}_{e,i}||\boldsymbol{\Gamma}_{e,j}|\alpha_{e}^{-1}\tau_{i}\underbrace{(\hat{\mathbf{u}}_{j}\cdot\boldsymbol{n}_{j})\hat{\boldsymbol{u}}_{j}}_{(\hat{\boldsymbol{u}}_{j}\otimes\hat{\boldsymbol{u}}_{j})\boldsymbol{n}_{j}} + |\boldsymbol{\Gamma}_{e,i}|\mathcal{X}_{\mathcal{N}e}(i)\underbrace{(\hat{\boldsymbol{u}}_{i}\cdot\boldsymbol{n}_{i})\hat{\boldsymbol{u}}_{i}}_{(\hat{\boldsymbol{u}}_{i}\otimes\hat{\boldsymbol{u}}_{i})\boldsymbol{n}_{i}} \tag{4.3.6}$$

Therefore, $(\hat{\mathbf{A}}_{\hat{u}\hat{u}})^{e}_{ij}$ reads as

$$\begin{aligned} (\hat{\mathbf{A}}_{\hat{u}\hat{u}})^{e}_{ij} = &- |\boldsymbol{\Gamma}_{e,i}||\boldsymbol{\Gamma}_{e,j}|\alpha_{e}^{-1}\tau_{i}(\hat{\mathbf{u}}_{j}\cdot\boldsymbol{n}_{j})\hat{\boldsymbol{u}}_{j} + |\boldsymbol{\Gamma}_{e,i}|\mathcal{X}_{\mathcal{N}e}(i)(\hat{\boldsymbol{u}}_{i}\cdot\boldsymbol{n}_{i})\hat{\boldsymbol{u}}_{i} \\ &- |\boldsymbol{\Gamma}_{e,i}||\boldsymbol{\Gamma}_{e,j}|\alpha_{e}^{-1}\tau_{i}(\hat{\mathbf{u}}_{j}\otimes\hat{\boldsymbol{u}}_{j})\boldsymbol{n}_{j} + |\boldsymbol{\Gamma}_{e,i}|\mathcal{X}_{\mathcal{N}e}(i)(\hat{\boldsymbol{u}}_{i}\otimes\hat{\boldsymbol{u}}_{i})\boldsymbol{n}_{i} \end{aligned} \tag{4.3.7}$$

The diagram in Figure (4.3) illustrates the procedure of solving the nonlinear system with Newton-Raphson method.

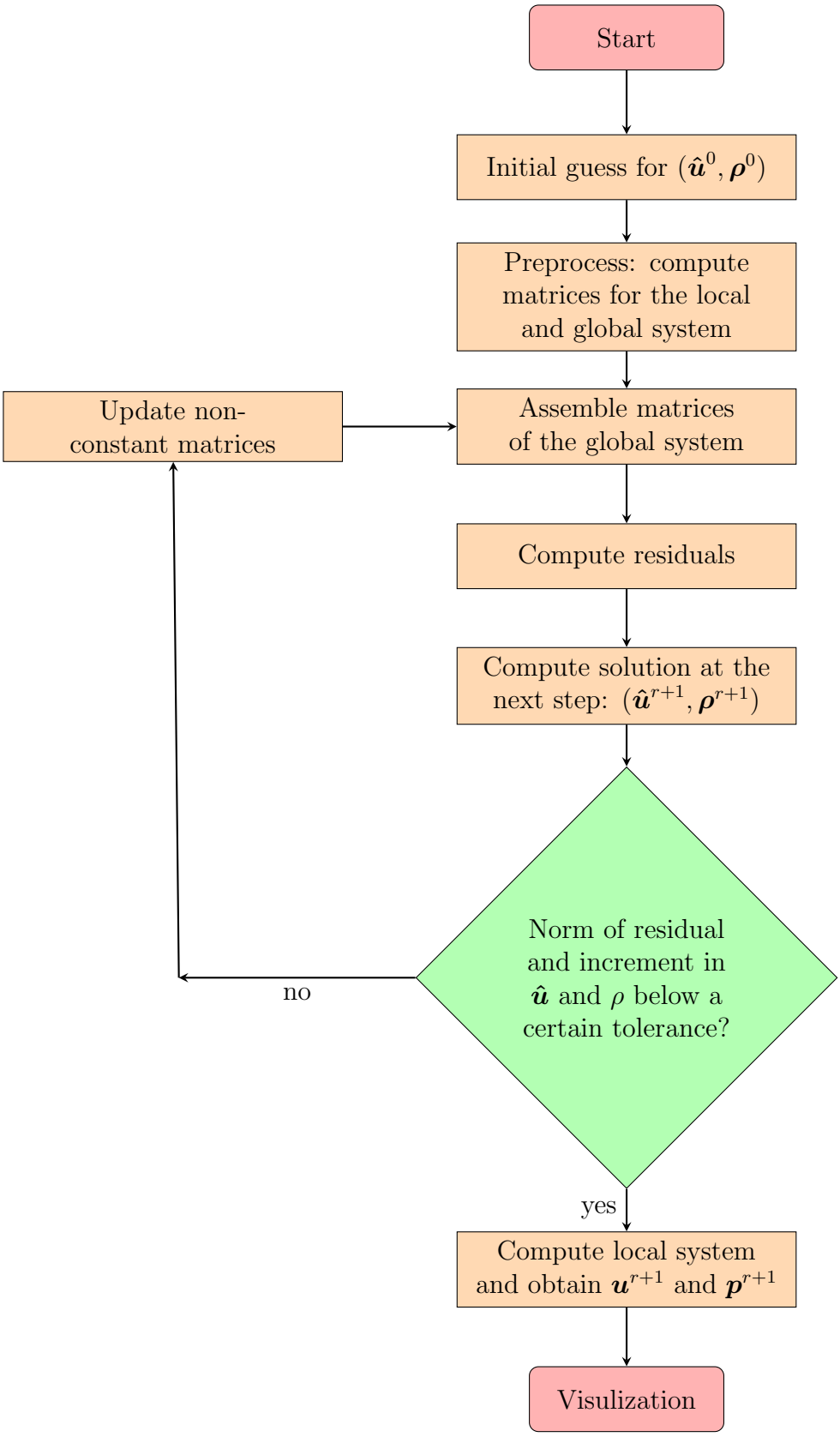
Start
Initial guess for $(\hat{\boldsymbol{u}}^0, \boldsymbol{\rho}^0)$
Preprocess: compute matrices for the local and global system
Assemble matrices of the global system
Update non-constant matrices
Compute residuals
Compute solution at the next step: $(\hat{\boldsymbol{u}}^{r+1}, \boldsymbol{\rho}^{r+1})$
Norm of residual and increment in $\hat{\boldsymbol{u}}$ and ρ below a certain tolerance?
no
yes
Compute local system and obtain $\boldsymbol{u}^{r+1}$ and $\boldsymbol{p}^{r+1}$
Visulization

4.4 Numerical studies

4.4.1 Rotating flow

In order to verify the convergence properties of the FCFV method for the Navier-Stokes equations, the same benchmark example of the rotating flow as in the section of the Oseen problem is simulated with all Dirichlet boundary conditions. The analytical expression of the velocity and pressure is:

$$\begin{cases} u_1(\boldsymbol{x}) = (1 - \cos(2\pi x)) \sin(2\pi y) \\ u_2(\boldsymbol{x}) = -\sin(2\pi x)(1 - \cos(2\pi y)) \\ p(\boldsymbol{x}) = \cos(\pi x) + \cos(\pi y) \end{cases} \tag{4.4.1}$$

in the square domain $\Omega = [0, 1]^2$, where the source term and boundary conditions are chosen to reproduce the above analytical solution.

Figure 4.1 and 4.2 demonstrate the velocity and pressure fields from the numerical solution. Compared with the analytical plots Figure 3.1, it can be observed that there exists great discrepancy in the pressure field when the mesh is coarse. Even though inaccurate pressure fields are obtained with fourth level meshes, if we refine the mesh to the eighth level the results are in good agreement with the analytical solutions.

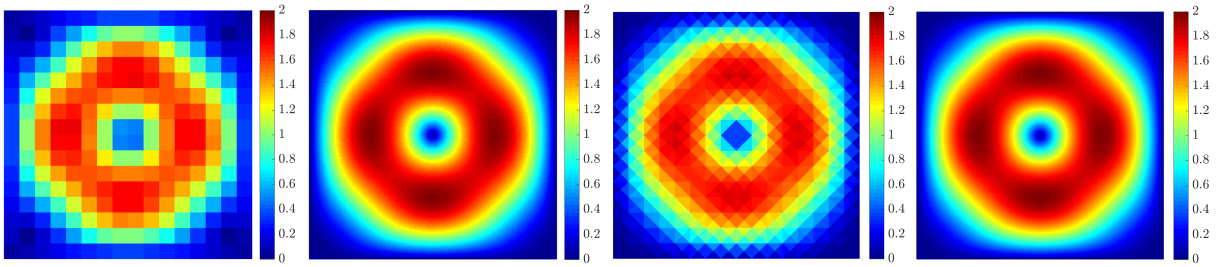

(a) QUA H4 (b) QUA H8 (c) TRI H4 (d) TRI H8

Figure 4.1: Numerical approximation of the module of velocity(QUA: quadrilateral mesh, TRI: triangular mesh; H4: fourth level refinement, H8: eighth level refinement)

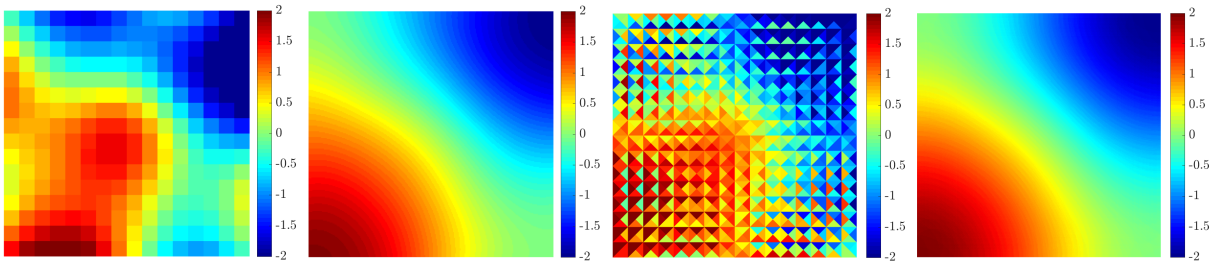

(a) QUA H4 (b) QUA H8 (c) TRI H4 (d) TRI H8

Figure 4.2: Numerical approximation of the pressure field (QUA: quadrilateral mesh, TRI: triangular mesh; H4: fourth level refinement, H8: eighth level refinement)

In this example, a constant convection stabilisation parameter is implemented over the domain. It is calculated from the $\mathcal{L}_2$ norm of the velocity field. Figure 4.3 shows the convergence rate of the rotating flow example with $\tau^d = 10\frac{\nu}{\ell}, \quad \tau^a = \|\boldsymbol{u}\|_{\mathcal{L}_2(\Omega)}$. The error in the velocity field is lower than the error in the pressure field. For the finest refinement mesh, the error of the velocity is less than 1% while that of the pressure is around 5%. Optimal convergence rates of all the variables are achieved for both triangular and quadrilateral meshes.

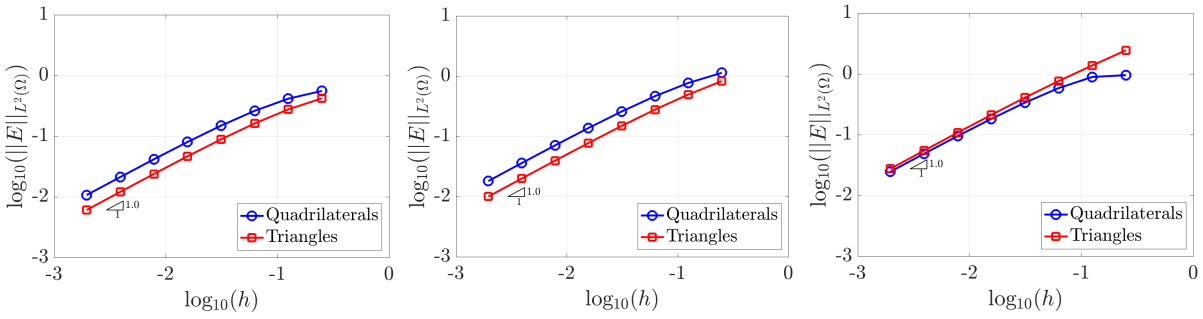

(a) $\boldsymbol{u}$ (b) $\boldsymbol{L}$ (c) p

Figure 4.3: Convergence rate of the rotating flow

4.4.2 2D lid-driven cavity flow

Another example considered is the lid-driven cavity flow, which is one of the standard benchmark test for incompressible flows [1, 41–43]. It models a plane flow of an isothermal fluid in a square lid-driven cavity. The upper side of the cavity moves along the boundary at unitary speed, whereas the other sides are fixed. In this section, we will apply the cavity flow example to check the applicability of the FCFV method to laminar incompressible Navier-Stokes flows. Since there is no analytical solution of this example, the results are compared with the reference data for validation.

The boundary conditions of the lid-driven cavity flow is shown in Figure 4.4. There are many possibilities to prescribe the boundary conditions. We can consider the corners belong to the upper side which leads to the leaky cavity problem. By doing this, there will be discontinuity in the velocity field at the two corners and it will cause the singularity in the pressure field [10].

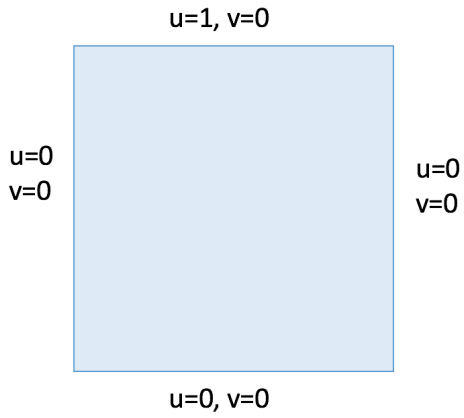

Figure 4.4: Boundary conditions of the lid-driven cavity flow

In order to avoid the singularity in the pressure field at the top corners, a non-leaky cavity problem with with a lumped velocity profile on the upper side is implemented, which dipicts a smooth transition of the velocity at the top corners . The transition function at the left corner is defined as $u = \sin(\frac{\pi}{d}(x - \frac{d}{2}))$ when $0 \leqslant x \leqslant d$ and that at the right corner $u = -\sin(\frac{\pi}{d}(x - 1 + \frac{d}{2}))$ when $1 - d \leqslant x \leqslant 1$, where d is the length of the transition region. In this case, we choose $d = 0.06$. Figure 4.5 illustrates the lumped velocity profiles defined for the non-leaky boundary conditions at the top of the cavity.

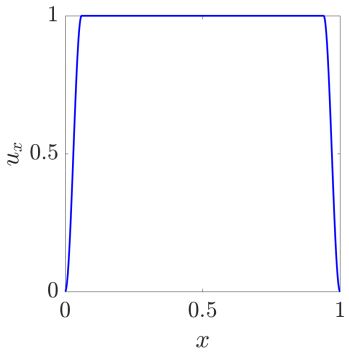

Figure 4.5: Velocity profiles at the top of the cavity

The cavity flow with different values of Reynolds number is analysed in this study for the

Re	h_c
100	0.0316
400	0.0112
1000	0.0056

Table 4.1: Characteristic size under different Reynold's number

verification of the FCFV method . The characteristic mesh size is chosen according to the Kolmogorov scale. The estimation for the ratio of the largest to smallest length scales in the flow is

$$\frac{l}{\eta} = R_e^{\frac{3}{4}} \tag{4.4.2}$$

where η is the size of the smallest eddies and l is the size of the largest eddies.
Therefore, the characteristic mesh size h_c should be smaller than $R_e^{-\frac{3}{4}}l$, where l is the characteristic length of the domain. Due to the low order approximation of the finite volume method, we need a fine enough mesh to capture the characteristics of the flow. Here we use sixth and eighth order structured triangular meshes to simulate the problem, whose largest sizes of the element are respectively 0.0156 and 0.0039. In this project, problems with R_e = 1-1000 are simulated. Three simulations are done with $R_e = 100$, $R_e = 400$ and $R_e = 1000$. The initial velocity field for the Newton-Raphson scheme is chosen to be all zeros for $R_e = 100$ and the results are reused as the initial condition of higher Reynolds number problems in order to accelerate the convergence of the Newton-Raphson method. In this case, we apply pointwise convection stabilisation parameter $\tau^a = 3\|\hat{\boldsymbol{u}}\|_2$, where $\hat{\boldsymbol{u}}$ is from the previous one in the Newton-Raphson iteration. The solution is compared with a reference solution from [1]. For higher Reynolds number such as $R_e = 10000$, a very fine mesh and a more advance linear solver is needed.

Figures 4.6-4.8 depict the velocity and pressure fields of the lid-driven cavity flow under different Reynolds numbers. As expected, the pressure rapidly increased from 0 to very high values because sudden change of velocity happens in this region. The figures of velocity fields shows that when the Reynolds number increases, the flow in the center of the domain is more stimulated and rotates faster. Two smaller vortexes are generated at the lower corners, where the module of velocity is close to 0. Moreover, the figure of the module of velocity at $Re = 1000$ also shows that finer meshes captures the rotation in the domain better than the coarser ones – the evolution of velocity in the finer mesh is more obvious. This implies that apart from a relatively fine mesh at the boundary, the size of mesh close to the center of the domain should also be chosen carefully in order to capture the primal vortex very well.

Another interesting flow characteristic is the position of the primary vortex. The discrepancy of the coarser mesh from the reference ones when dealing with higher Reynolds number is also shown in Table 4.4.2 and the plots of the velocity at the horizontal and vertical central lines. Table 4.4.2 compare the results from the present study with those in the existing literature. As the Reynolds number increases, the position of the primary

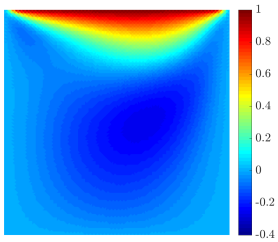

(a) H6 $Re = 100$

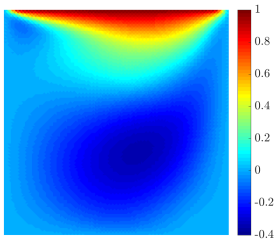

(b) H6 $Re = 400$

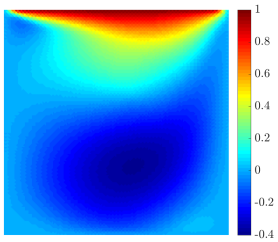

(c) H6 $Re = 1000$

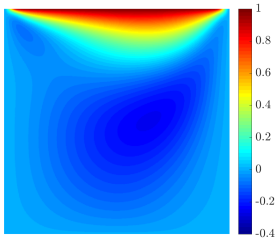

(d) H8 $Re = 100$

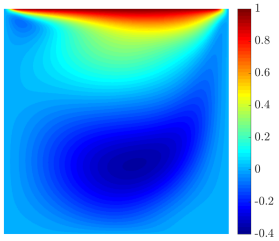

(e) H8 $Re = 400$

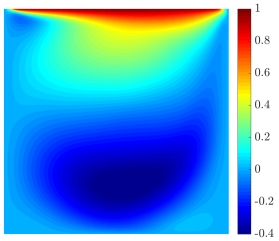

(f) H8 $Re = 1000$

Figure 4.6: Comparison of u_1 fields of different Reynolds numbers

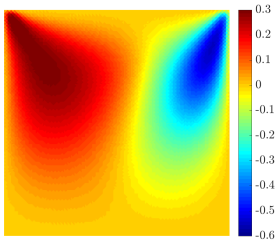

(a) H6 $Re = 100$

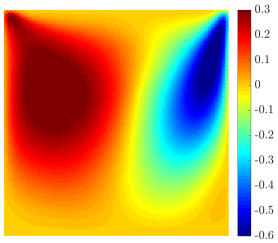

(b) H6 $Re = 400$

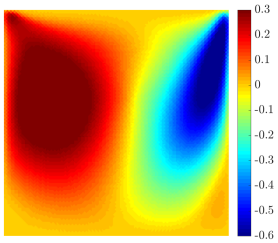

(c) H6 $Re = 1000$

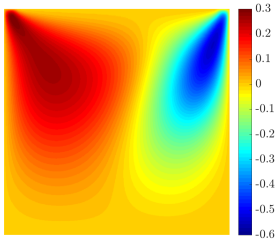

(d) H8 $Re = 100$

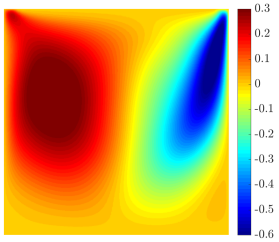

(e) H8 $Re = 400$

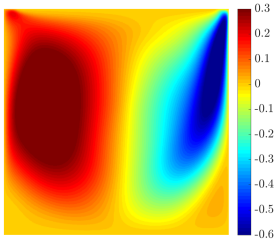

(f) H8 $Re = 1000$

Figure 4.7: Comparison of u_2 fields of different Reynolds numbers

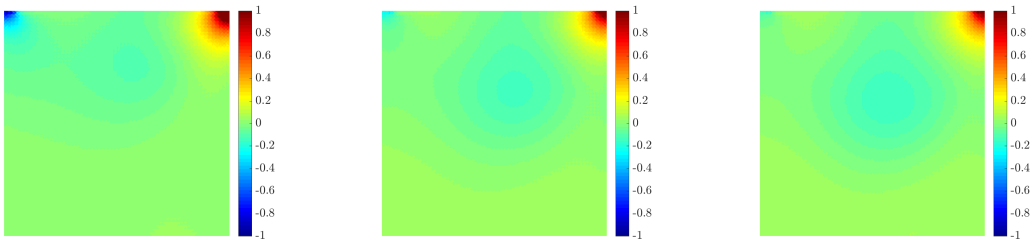

(a) H6 $Re = 100$ (b) H6 $Re = 400$ (c) H6 $Re = 1000$

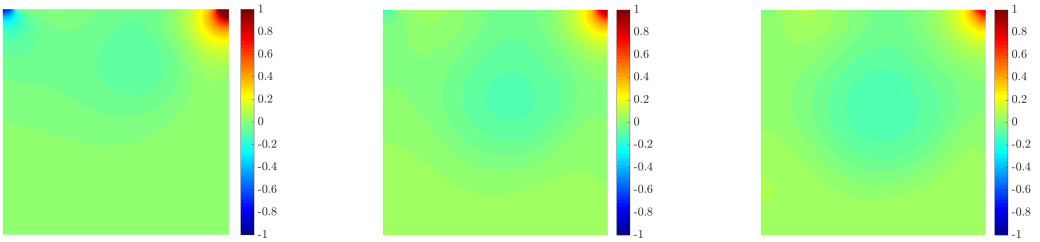

(d) H8 $Re = 100$ (e) H8 $Re = 400$ (f) H8 $Re = 1000$

Figure 4.8: Comparison of pressure fields of different Reynolds numbers

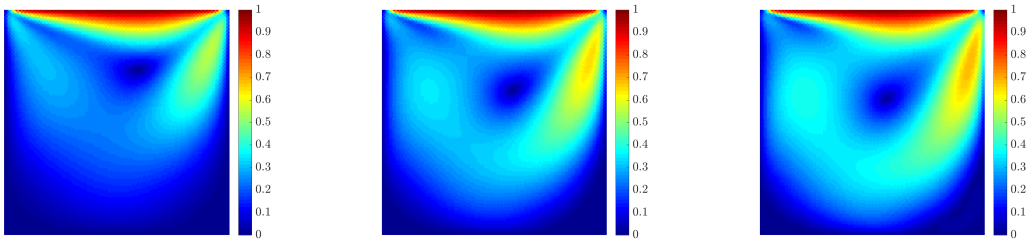

(a) H6 $Re = 100$ (b) H6 $Re = 400$ (c) H6 $Re = 1000$

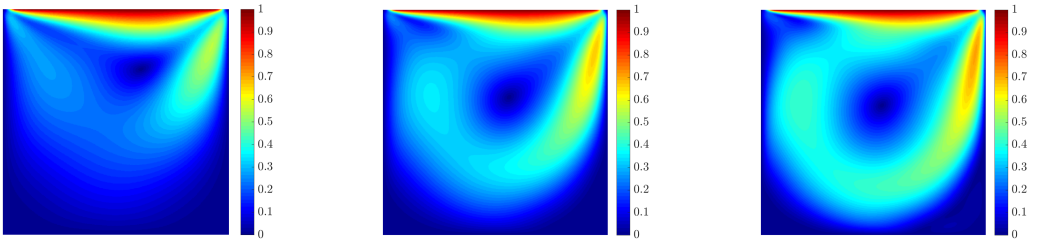

(d) H8 $Re = 100$ (e) H8 $Re = 400$ (f) H8 $Re = 1000$

Figure 4.9: Comparison of $\|\boldsymbol{u}\|_2$ fields of different Reynolds numbers

vortex moves closer to the center of the domain. The relative deviation of the results calculated with the eighth order triangular mesh of current study from the reference ones (Ghia et al. [1]) is lower than 2% with the given different Reynolds numbers, which shows good agreement with the literature.

Reference	$Re = 100$	$Re = 400$	$Re = 1000$
Present study (TRIH6)	(0.60738,0.73492)	(0.58611,0.64208)	(0.56511,0.60673)
Present study (TRIH8)	(0.61074,0.73489)	(0.56151,0.61294)	(0.54023,0.57386)
Donea and Huerta [10]	(0.62,0.74)	(0.568,0.606)	(0.540,0.573)
Ghia et al. [1]	(0.6172,0.7344)	(0.5547,0.6055)	(0.5313,0.5625)
Khorasanizade et al. [41]	(0.6178, 0.7401)	(0.5568,0.6066)	(0.5396, 0.5742)
Karakashian et al. [44]	(0.6178, 0.7502)	(0.5589,0.6025)	(0.5336, 0.5666)

Table 4.2: Position of the primary vortex at different Reynolds numbers compared with values from the references

The evolution of vortexes can be visualized in Figure 4.10. As we can see in the figure, the main vortex appears on the upper right part of the domain. As the Reynolds number increases, it moves towards the center, which is correspondent to what we have observed from Table 4.4.2. Moreover, the revolution of the flow becomes more severe and the size of the smaller vortexes at the lower corners gets larger.

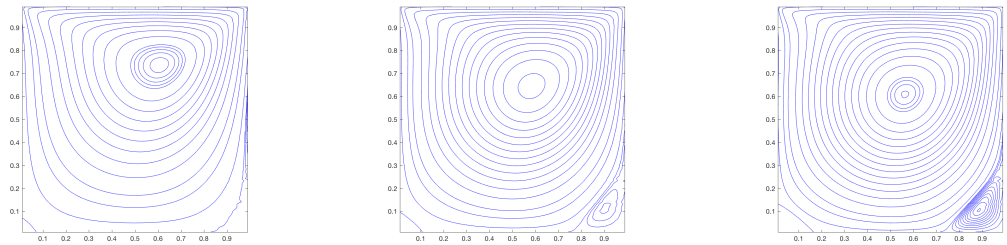

(a) H6 $Re = 100$ (b) H6 $Re = 400$ (c) H6 $Re = 1000$

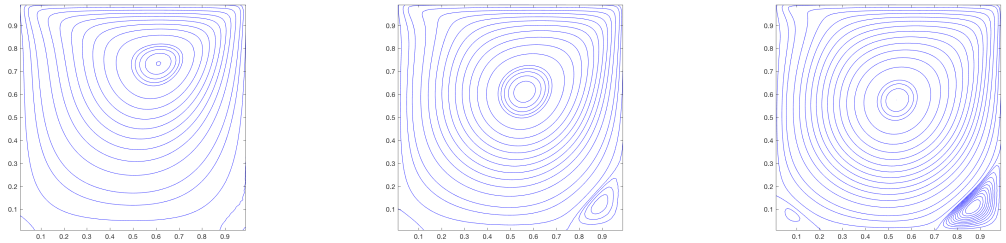

(d) H8 $Re = 100$ (e) H8 $Re = 400$ (f) H8 $Re = 1000$

Figure 4.10: Comparison of streamlines of the cavity flow under different values of Reynolds number

Figure 4.11 and 4.12 show the comparison of central line velocities with the reference data. Overall, the results from the current study are in good agreement with the reference data, but noticeable discrepancies can still be observed near the four cavity walls, especially for higher Reynolds numbers. This is due to the fact that the viscous effect near the boundary are more influential when Reynolds number increases. It can be seen that, the thickness of boundary layer of $Re = 1000$ is smaller than 0.05. Therefore it requires a finer mesh at the boundaries in order to capture the sharp change of velocity there.

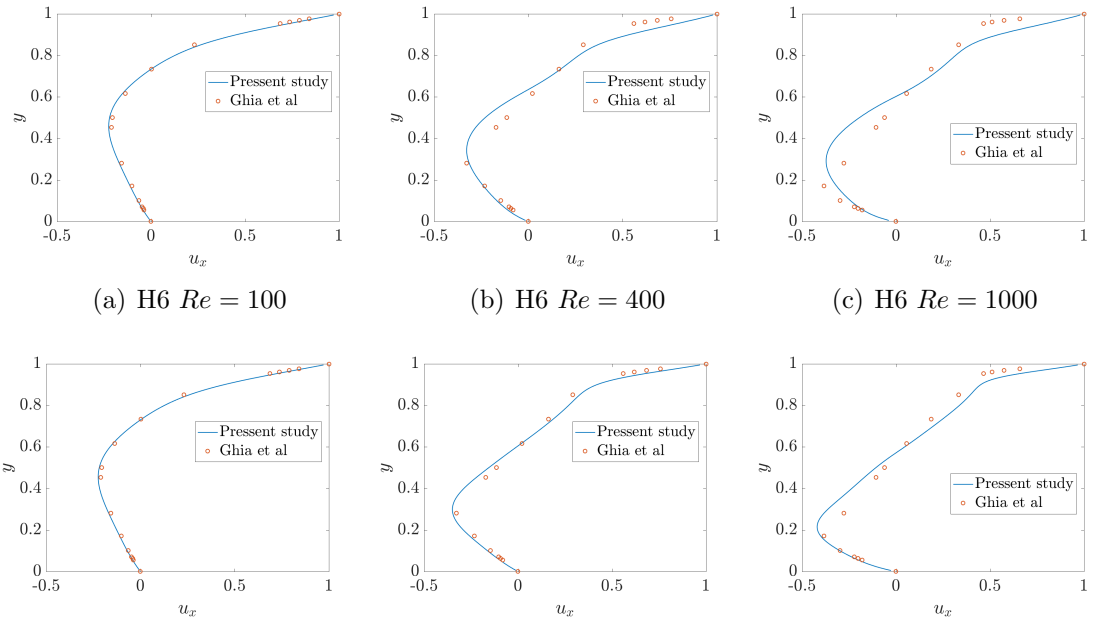

(a) H6 $Re = 100$ (b) H6 $Re = 400$ (c) H6 $Re = 1000$

(d) H8 $Re = 100$ (e) H8 $Re = 400$ (f) H8 $Re = 1000$

Figure 4.11: Velocity profiles along vertical central lines for Re = 100, 400, 1000 calculated with sixth(top) and eighth(bottom) level meshes compared with the results of Ghia et al. [1]

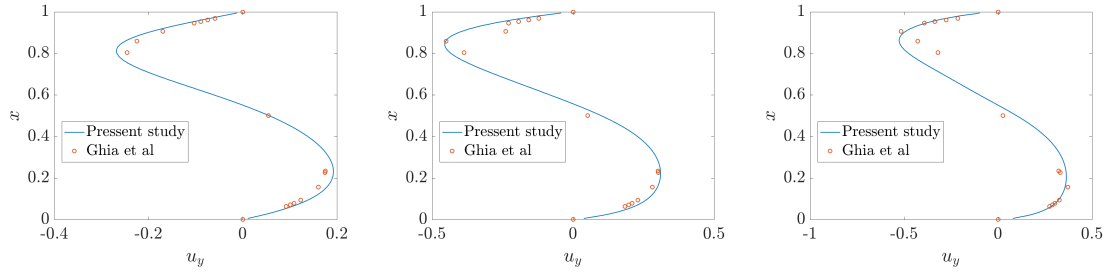

(a) H6 $Re = 100$ (b) H6 $Re = 400$ (c) H6 $Re = 1000$

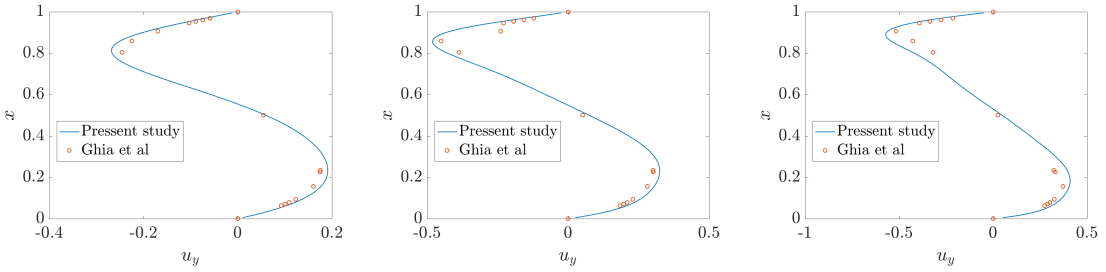

(d) H8 $Re = 100$ (e) H8 $Re = 400$ (f) H8 $Re = 1000$

Figure 4.12: Velocity profiles along horizontal central lines for Re = 100, 400, 1000 calculated with sixth(top) and eighth(bottom) level meshes compared with the results of Ghia et al. [1]

All in all, the results of the uniform mesh are in good agreement with the reference data. However, they are quite computationally expensive because all the elements need to be of the size of the elements in the boundary layer. When the Reynolds number is very high, the scale of the problem is difficult to deal with. This can be solved with the introduction of boundary layer meshes. Far away from the boundaries, a relatively coarser mesh is used in order to obtain accurate results under acceptable computational cost. Figure 4.13 shows the mesh for the following simulation when $R_e = 1000$. The thickness of the first boundary layer of the mesh is 0.001 and the size of the element far way from the boundary is 0.005. The scale of this problem is reduced to less than one fifth of that of the above one. The number of elements in the mesh with boundary layers is 41,000 while that of the eighth level structured triangular mesh is 262,000. Three vortexes can be seen in Figure 4.15. The position of the main vortex calculated by this mesh is $(0.547, 0.57385)$. Compared with the results of Ghia et al [1], the relative discrepancy is only around 1%, which is acceptable under engineering tolerance. Moreover, if we compare the velocities at the central lines, the mesh with boundary layers can capture very well the sharp gradient of u_x at vertical central lines and u_y at horizontal central lines. For u_x it is even slightly better than the results from the eighth level uniform mesh while the computational cost is much smaller. It can be concluded that the boundary layer plays an important role in higher Reynolds number problems. It is preferable to use meshes with boundary layers for simulation to increase the accuracy under acceptable computational cost.

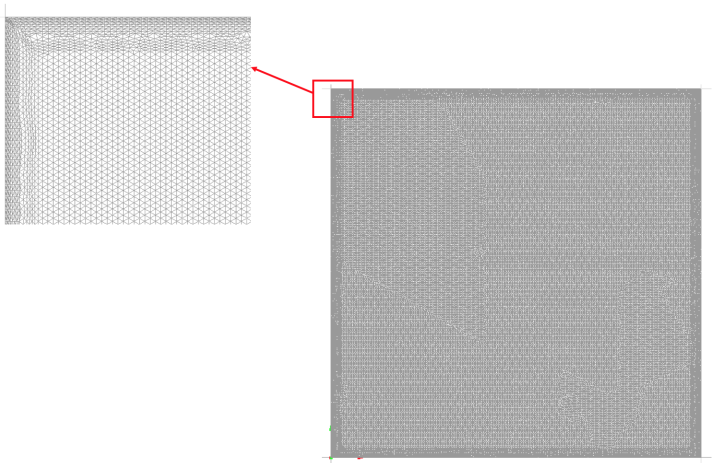

Figure 4.13: Refined mesh at boundaries

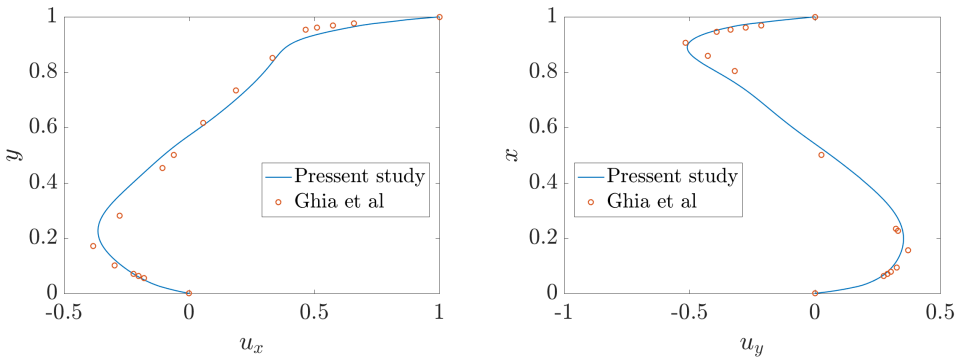

Figure 4.14: Velocity profiles along vertical (left) and horizontal (right) central lines for Re = 1000 calculated with the mesh with boundary layers compared with the results of Ghia et al. [1]

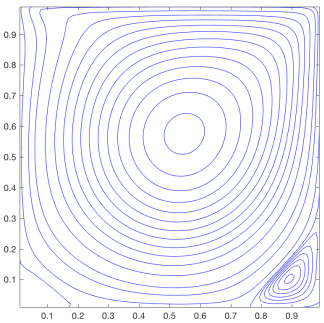

Figure 4.15: Streamlines for Re = 1000 calculated with the mesh with boundary layers

Chapter 5

Conclusion

This project presents a finite volume solver for steady incompressible Navier-Stokes equations – the face-centered finite volume method (FCFV). FCFV defines unknowns on the faces of the mesh and may be interpreted as a lowest-order HDG discretization, from which it inherits optimal convergence properties for all the variables under analysis. Detailed description of the method is demonstrated with three types of equations – the Stokes, Oseen and incompressible Navier-Stokes equations. Voigt notation is utilized in order to enforce the symmetry of the stress tensor.

The FCFV method for the Stokes equations gives accurate results and optimal first-order convergence rate is obtained for velocity, pressure and strain tensor. These results are confirmed in presence of convection, both linear (Oseen equations) and nonlinear (Navier-Stokes equations). Moreover, a sensitivity study showing the robustness of the method to the choice of the stabilization parameters is performed.

The lid-driven cavity flow example is tested for the analysis of the efficiency of the method. The simulations at different low Reynolds number are in good agreement with the results from the literature. For higher Reynolds numbers, fine meshes are needed to achieve acceptable accuracy and the scale of the problem gets quite larger, especially in 3D. In this case, the direct solver will go beyond memory limitation. A remedy for it is the application of iterative solvers. However, the iterative solvers available in MATLAB®, such as GMRES, MINRES and BICG, are not very well suited to solve saddle-point problems. For an incompressible Navier-Stokes problem, the saddle point problem need to be solved and the matrix is neither symmetric or positive definite. These solvers will struggle a lot to solve the final system of equations. Special solvers developed for saddle point problems should be exploited such as Uzawa iterative method [45]. Moreover, using a parallel iterative solver will also improve the efficiency of solving a large-scale problem. The current FCFV framework can also be extended to the time-dependent problem. Many strategies for time discretization are available such as backward differentiation formulas, Runge-Kutta methods and DIRK methods [46].

Bibliography

[1] U. Ghia, K. N. Ghia, and C. Shin, "High-re solutions for incompressible flow using the navier-stokes equations and a multigrid method," *Journal of computational physics*, vol. 48, no. 3, pp. 387–411, 1982.

[2] H. Versteeg and W. Malalasekera, "An introduction to computational fluid dynamics : the finite volume method / h. k. versteeg and w. malalasekera.," *SERBIULA (sistema Librum 2.0)*, 06 2019.

[3] I. Demirdžić and S. Muzaferija, "Numerical method for coupled fluid flow, heat transfer and stress analysis using unstructured moving meshes with cells of arbitrary topology," *Computer methods in applied mechanics and engineering*, vol. 125, no. 1-4, pp. 235–255, 1995.

[4] C. Bailey and M. Cross, "A finite volume procedure to solve elastic solid mechanics problems in three dimensions on an unstructured mesh," *International journal for numerical methods in engineering*, vol. 38, no. 10, pp. 1757–1776, 1995.

[5] C. H. Lee, A. J. Gil, and J. Bonet, "Development of a cell centred upwind finite volume algorithm for a new conservation law formulation in structural dynamics," *Computers & Structures*, vol. 118, pp. 13–38, 2013.

[6] B. Diskin, J. L. Thomas, E. J. Nielsen, H. Nishikawa, and J. A. White, "Comparison of node-centered and cell-centered unstructured finite-volume discretizations: viscous fluxes," *AIAA journal*, vol. 48, no. 7, pp. 1326–1338, 2010.

[7] B. Diskin and J. L. Thomas, "Comparison of node-centered and cell-centered unstructured finite-volume discretizations: inviscid fluxes," *AIAA journal*, vol. 49, no. 4, pp. 836–854, 2011.

[8] B. Diskin and J. Thomas, "Effects of mesh regularity on accuracy of finite-volume schemes," in *50th AIAA aerospace sciences meeting including the new horizons forum and aerospace exposition*, p. 609, 2012.

[9] T. Barth, R. Herbin, and M. Ohlberger, "Finite volume methods: foundation and analysis," *Encyclopedia of Computational Mechanics Second Edition*, pp. 1–60, 2018.

[10] J. Donea and A. Huerta, *Finite element methods for flow problems*. John Wiley & Sons, 2003.

[11] C. A. Felippa, "Introduction to finite element methods," *Course Notes, Department of Aerospace Engineeing Sciences, University of Colorado at Boulder, available at http://www. colorado. edu/engineering/Aerospace/CAS/courses. d/IFEM. d*, 2004.

[12] O. Pironneau and O. Pironneau, *Finite element methods for fluids*. Wiley Chichester, 1989.

[13] P. Hood and C. Taylor, "Navier-stokes equations using mixed interpolation," *Finite element methods in flow problems*, pp. 121–132, 1974.

[14] R. Stenberg, "Analysis of mixed finite elements methods for the stokes problem: a unified approach," *Mathematics of computation*, vol. 42, no. 165, pp. 9–23, 1984.

[15] R. Temam, *Navier-Stokes equations: theory and numerical analysis*, vol. 343. American Mathematical Soc., 2001.

[16] V. Girault and P.-A. Raviart, *Finite element methods for Navier-Stokes equations: theory and algorithms*, vol. 5. Springer Science & Business Media, 2012.

[17] O. C. Zienkiewicz and P. Godbole, "A penalty function approach to problems of plastic flow of metals with large surface deformations," *Journal of Strain Analysis*, vol. 10, no. 3, pp. 180–183, 1975.

[18] G. N. Gatica, L. F. Gatica, and A. Márquez, "Augmented mixed finite element methods for a vorticity-based velocity–pressure–stress formulation of the stokes problem in 2d," *International Journal for Numerical Methods in Fluids*, vol. 67, no. 4, pp. 450–477, 2011.

[19] G. N. Gatica, A. Márquez, R. Oyarzúa, and R. Rebolledo, "Analysis of an augmented fully-mixed approach for the coupling of quasi-newtonian fluids and porous media," *Computer Methods in Applied Mechanics and Engineering*, vol. 270, pp. 76–112, 2014.

[20] J. Camaño, R. Oyarzúa, and G. Tierra, "Analysis of an augmented mixed-fem for the navier-stokes problem," *Mathematics of Computation*, vol. 86, no. 304, pp. 589–615, 2017.

[21] R. M. Beam and H. E. Bailey, "Newton's method for the navier-stokes equations," in *Computational Mechanics' 88*, pp. 1457–1460, Springer, 1988.

[22] A. Segal and C. Vuik, *A simple iterative linear solver for the 3D incompressible Navier-Stokes equations discretized by the finite element method*. Delft University of Technology, Faculty of Technical Mathematics and Informatics, 1995.

[23] J. N. Shadid, R. S. Tuminaro, and H. F. Walker, "An inexact newton method for fully coupled solution of the navier–stokes equations with heat and mass transport," *Journal of Computational Physics*, vol. 137, no. 1, pp. 155–185, 1997.

[24] W. H. Reed and T. Hill, "Triangular mesh methods for the neutron transport equation," tech. rep., Los Alamos Scientific Lab., N. Mex.(USA), 1973.

[25] B. Cockburn and J. Gopalakrishnan, "A characterization of hybridized mixed methods for second order elliptic problems," *SIAM Journal on Numerical Analysis*, vol. 42, no. 1, pp. 283–301, 2004.

[26] B. Cockburn and J. Gopalakrishnan, "Incompressible finite elements via hybridization. part i: The stokes system in two space dimensions," *SIAM Journal on Numerical Analysis*, vol. 43, no. 4, pp. 1627–1650, 2005.

[27] B. Cockburn and J. Gopalakrishnan, "New hybridization techniques," *GAMM-Mitteilungen*, vol. 28, no. 2, pp. 154–182, 2005.

[28] B. Cockburn, J. Gopalakrishnan, and R. Lazarov, "Unified hybridization of discontinuous galerkin, mixed, and continuous galerkin methods for second order elliptic problems," *SIAM Journal on Numerical Analysis*, vol. 47, no. 2, pp. 1319–1365, 2009.

[29] R. Sevilla, M. Giacomini, A. Karkoulias, and A. Huerta, "A superconvergent hybridisable discontinuous galerkin method for linear elasticity," *International Journal for Numerical Methods in Engineering*, vol. 116, no. 2, pp. 91–116, 2018.

[30] R. Sevilla, M. Giacomini, and A. Huerta, "A locking-free face-centred finite volume (fcfv) method for linear elastostatics," *Computers & Structures*, vol. 212, pp. 43–57, 2019.

[31] A. C. Limache and S. R. Idelsohn, "Laplace form of navier-stokes equations: A safe path or a wrong way?," *Mecánica Computacional*, vol. 137, no. 25, 2006.

[32] M. Giacomini, A. Karkoulias, R. Sevilla, and A. Huerta, "A superconvergent hdg method for stokes flow with strongly enforced symmetry of the stress tensor," *Journal of Scientific Computing*, vol. 77, no. 3, pp. 1679–1702, 2018.

[33] J. Fish and T. Belytschko, *A first course in finite elements*, vol. 1. John Wiley & Sons New York, 2007.

[34] A. Montlaur, S. Fernandez-Mendez, and A. Huerta, "Discontinuous galerkin methods for the stokes equations using divergence-free approximations," *International journal for numerical methods in fluids*, vol. 57, no. 9, pp. 1071–1092, 2008.

[35] B. Cockburn and J. Cui, "An analysis of hdg methods for the vorticity-velocity-pressure formulation of the stokes problem in three dimensions," *Mathematics of Computation*, vol. 81, no. 279, pp. 1355–1368, 2012.

[36] N. C. Nguyen, J. Peraire, and B. Cockburn, "A hybridizable discontinuous galerkin method for stokes flow," *Computer Methods in Applied Mechanics and Engineering*, vol. 199, no. 9-12, pp. 582–597, 2010.

[37] J. Vila Perez, "Hi-fi hybridisable discontinuous galerkin method for incompressible flows," Master's thesis, Universitat Politècnica de Catalunya, 2017.

[38] J. M. Hoermann, C. Bertoglio, M. Kronbichler, M. R. Pfaller, R. Chabiniok, and W. A. Wall, "An adaptive hybridizable discontinuous galerkin approach for cardiac electrophysiology," *International Journal for Numerical Methods in Biomedical Engineering*, vol. 34, no. 5, p. e2959, 2018.

[39] B. Cockburn and J. Shen, "An algorithm for stabilizing hybridizable discontinuous galerkin methods for nonlinear elasticity," *Results in Applied Mathematics*, p. 100001, 2019.

[40] N. C. Nguyen, J. Peraire, and B. Cockburn, "An implicit high-order hybridizable discontinuous galerkin method for linear convection–diffusion equations," *Journal of Computational Physics*, vol. 228, no. 9, pp. 3232–3254, 2009.

[41] S. Khorasanizade and J. M. Sousa, "A detailed study of lid-driven cavity flow at moderate reynolds numbers using incompressible sph," *International Journal for Numerical Methods in Fluids*, vol. 76, no. 10, pp. 653–668, 2014.

[42] S. Hou, Q. Zou, S. Chen, G. Doolen, and A. C. Cogley, "Simulation of cavity flow by the lattice boltzmann method," *Journal of computational physics*, vol. 118, no. 2, pp. 329–347, 1995.

[43] O. Botella and R. Peyret, "Benchmark spectral results on the lid-driven cavity flow," *Computers & Fluids*, vol. 27, no. 4, pp. 421–433, 1998.

[44] O. Karakashian and T. Katsaounis, "Numerical simulation of incompressible fluid flow using locally solenoidal elements," *Computers & Mathematics with Applications*, vol. 51, no. 9-10, pp. 1551–1570, 2006.

[45] H. Uzawa, "Optimum technical change in an aggregative model of economic growth," *International economic review*, vol. 6, no. 1, pp. 18–31, 1965.

[46] P. Birken, "Numerical methods for the unsteady compressible navier-stokes equations," 2012.